

# Polarization Lidar: Principles and Applications

Xudong Liu <sup>1,2</sup>, Liping Zhang <sup>3</sup>, Xiaoyu Zhai <sup>4</sup>, Liye Li <sup>5</sup>, Qingji Zhou <sup>1</sup>, Xue Chen <sup>6,\*</sup> and Xiaobo Li <sup>1,2,\*</sup> 

- <sup>1</sup> School of Marine Science and Technology, Tianjin University, Tianjin 300054, China; sunny777@tju.edu.cn (X.L.); zqj@tju.edu.cn (Q.Z.)  
<sup>2</sup> College of Mechanical Engineering and Automation, Fuzhou University, Fuzhou 350108, China  
<sup>3</sup> Department of Imaging and Interventional Radiology, The Chinese University of Hong Kong, Hong Kong 999077, China; lpzhang@cuhk.edu.hk  
<sup>4</sup> National Ocean Technology Center, Tianjin 300112, China; cynthiachai@126.com  
<sup>5</sup> China Ship Scientific Research Center, Wuxi 214082, China; lly850189@163.com  
<sup>6</sup> Law School, Tianjin University, Tianjin 300054, China  
\* Correspondence: xuechen@tju.edu.cn (X.C.); lixiaobo@tju.edu.cn (X.L.)

**Abstract:** Traditional lidar techniques mainly rely on the backscattering/echo light intensity and spectrum as information sources. In contrast, polarization lidar (P-lidar) expands the dimensions of detection by utilizing the physical property of polarization. By incorporating parameters such as polarization degree, polarization angle, and ellipticity, P-lidar enhances the richness of physical information obtained from target objects, providing advantages for subsequent information analysis. Over the past five decades, the application fields of P-lidar have rapidly expanded, starting from its early use in atmospheric remote sensing to later applications in oceanic remote sensing. This review first provides a brief introduction to the basic principles of both polarization and P-lidar, along with typical systems. It then explores the applications of P-lidar in various remote sensing fields, including atmospheric, oceanic, and terrestrial domains. Additionally, we propose potential research directions based on current cutting-edge applications, with the aims of providing critical insights to researchers in the fields of polarization and lidar and inspiring further exciting ideas.

**Keywords:** polarization; lidar; remote sensing; P-lidar



**Citation:** Liu, X.; Zhang, L.; Zhai, X.; Li, L.; Zhou, Q.; Chen, X.; Li, X. Polarization Lidar: Principles and Applications. *Photonics* **2023**, *10*, 1118. <https://doi.org/10.3390/photronics10101118>

Received: 19 September 2023  
Revised: 1 October 2023  
Accepted: 2 October 2023  
Published: 4 October 2023



**Copyright:** © 2023 by the authors. Licensee MDPI, Basel, Switzerland. This article is an open access article distributed under the terms and conditions of the Creative Commons Attribution (CC BY) license (<https://creativecommons.org/licenses/by/4.0/>).

## 1. Introduction

Polarization, akin to parameters such as frequency, phase, and amplitude/intensity, represents a fundamental physical property of light [1–3]. The earliest records of polarized light can be traced back to 1669, when Bartholin discovered the phenomenon of double-refraction in a piece of Iceland spar (calcite), which paved the way for human exploration of polarized optics [2]. Subsequently, in 1678, Huygens proposed the wave theory of light, providing a satisfactory explanation for the polarization characteristics of light [2]. Therefore, Huygens is recognized as the first scientist in the history of physics to discover the properties of polarized light.

Polarized light is prevalent in the natural world, primarily resulting from reflection and scattering processes. This is because reflection and scattering often induce varying optical efficiencies and/or phase changes for the orthogonal polarization components of the incident light [3,4]. Consequently, differences in the surface structure and texture of an object can influence the polarization state of reflected and/or scattered light [5,6]. By measuring the polarization characteristics of reflected or scattered light, the analysis of surface morphology information becomes possible, leading to extensive applications of polarized light in remote sensing [7,8]. For example, in passive remote sensing, the polarization characteristics of solar spectral lines serve as important carriers for navigation [9,10]; when sunlight interacts with water vapor, ice crystals, dust, sand, smoke, and other substances, polarized light can be generated, proving the physical properties of such materials [11,12]. Furthermore, polarized light plays a significant role in areas including resource exploration, vegetation and soil

classification, research on the sea surface, and global atmospheric aerosol studies [5,13]. In active remote sensing, polarized light is indispensable for detecting aerosols' shape, identifying cloud phases, and determining particles' orientation [14–16].

In 1916, Einstein proposed the theory of light's stimulated emission (LSE) [17], which guided humanity to recognize such light with a precise single color and wavelength, which is also named light amplification by stimulated emissions of radiation (laser) [18]. However, it was not until 1960 that the first laser generator was developed, marking the beginning of laser utilization [19]. Actually, the idea of using a laser in radar systems, i.e., light detection and ranging (Lidar), was immediately considered after the laser's invention [20]. For instance, in 1969, an American team installed a retro-reflector device similar to a mirror on the lunar surface. Laser beams were directed towards this device from Earth, enabling accurate measurement of the Earth–Moon distance [21,22]. However, lasers quickly expanded beyond this application and found widespread utility in various fields, including surveying, atmospheric remote sensing, and oceanic remote sensing.

Lidar systems consist of three main components: transmitter, receiver, and processing. The transmitter emits a laser beam into a target scene, initiating an interaction between the laser and the target object (such as suspended particles in the atmosphere or seawater), which causes changes in various aspects of the optical signal, including propagation direction, intensity, frequency, polarization, and phase [23]. By detecting these changes and combining transmission models, information related to the target's physical properties, such as its position, velocity, and composition, can be inferred [24,25]. Figure 1 presents the basic elements of lidar: the laser sources, ranging principles, beam modulations, and detectors. It should be noted that all the used abbreviations and the related full definitions are listed in Appendix A.

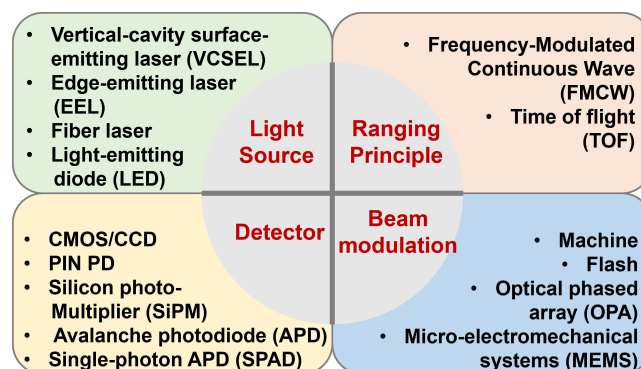
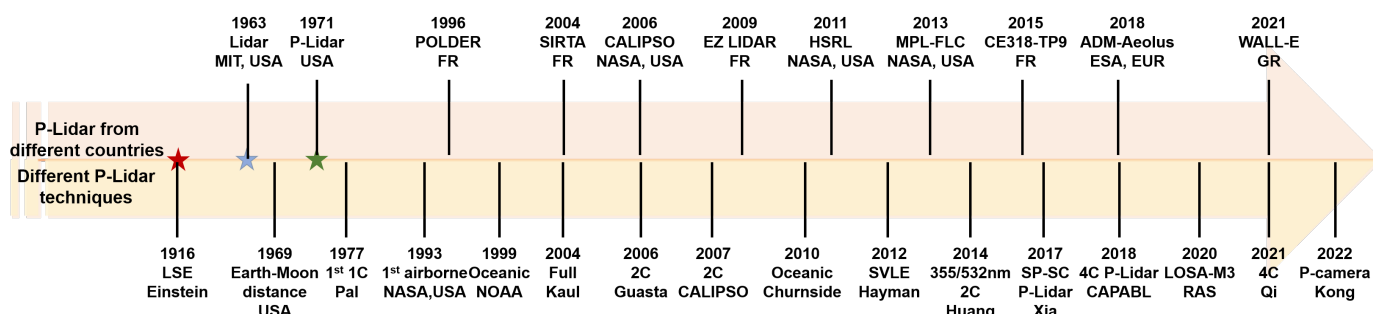


Figure 1. Basic components of lidar.

Lidar is a remote sensing technology similar to radar, which uses laser pulses as the radiation source instead of continuous electromagnetic waves. Commonly used laser sources include vertical-cavity surface-emitting lasers (VCSELs) [26], edge-emitting lasers (EELs) [27], fiber lasers, and light-emitting diodes (LEDs) [28]. It is worth noting that both pulsed and continuous-wave lasers are employed in lidar systems, where the pulsed systems measure the round-trip time of a short light pulse from the laser to the target and back to the receiver, i.e., the ranging principle is named time of flight (TOF) [29]; the continuous wave systems range by measuring the phase difference between the transmitted and received signals, for example the frequency-modulated continuous wave (FMCW) [30]. In lidar systems, three different wavelength regions are used: near-infrared (NIR) excitation at 1064 nm using diode-flashlamp-pumped solid-state or thulium-doped fiber lasers, visible light (VIS) excitation at 532 nm generated through frequency doubling of the 1064 nm laser or ultraviolet (UV) at 355 nm through frequency tripling, and short-wave infrared (SWIR) excitation at 1550 nm using erbium-doped fiber lasers. The advantages and disadvantages of these choices depend on the target reflectance and absorption, background radiation, atmospheric transmission, and eye safety considerations. According to the different ways

the laser beam is emitted towards the targets, lidar can be roughly divided into flash lidar and scanning lidar. Flash lidar systems observe the complete field of view (FOV) simultaneously and often employ a charge-coupled device (CCD) or complementary metal-oxide semiconductor (CMOS) sensors as detection devices [31]. Conversely, scanning lidar systems focus on a subset of the FOV before moving on to the next subset, covering the entire FOV sequentially. Scanning lidar systems have the ability to detect objects at greater area compared to flash lidar systems since the laser beam is concentrated on a subset of the FOV at a time [32]. However, the laser beam of the scanner necessitates redirection from one subset to another to cover the entire FOV. Current systems typically use mechanical-beam-steering principles, achieved either by rotating the entire sensor head (rotational lidar) or using internal micro-electromechanical systems (MEMS) within the sensor for beam steering. In this case, the detector may be a single-point detector, such as the PIN photodiode (PD) [33], silicon photo-multiplier (SiPM) [34], avalanche photodiode (APD), or single-photon APD (SPAD) [35]. More information about lidar’s basic components can be found in previous reviews [32,36–38].

Initially, lidar only detected intensity (or power) changes of backscattering or echo light signals; later, wavelength and/or frequency modulation was added; then, polarization modulation was introduced, forming polarization lidar, i.e., P-lidar. Researchers [39] from New York University initially borrowed the P-lidar technique from the microwave radar methods, which were developed in about the 1950s (before the laser was invented). They found that laser depolarization is considerably stronger compared to microwave depolarization from non-spherical particles, suggesting that P-lidar is more promising for studying aerosols, particles in clouds, and precipitation (i.e., hydrometeors). Polarization has become a crucial aspect in contemporary radar systems, with most systems incorporating polarization components to enable either the partial or complete functionality of P-lidar. A concise chronological chart of P-lidar (including spaceborne P-lidar launched by different countries and various P-lidar technologies) is presented in Figure 2.



**Figure 2.** History of P-lidar. 1C: single-channel; 2C: dual-channel; 4C: four-channel; SP: single-photon; other abbreviations can be found in the main text. The corresponding references for the second line are [17,21,22,40–55].

In terms of applications, according to the Mie scattering theory [56], when polarized light is incident on spherical particles (such as water droplets), the backscattered light is in the same polarization state as the emitted light. However, when polarized light is incident on non-spherical particles (such as ice crystals), a portion of the backscattered light becomes depolarized, resulting in partially polarized light. By analyzing the changes in the echo signal’s polarization state, P-lidar can distinguish between spherical and non-spherical particles in the atmosphere [15]. As a result, P-lidar was initially widely used for identifying liquid water clouds and ice clouds in the atmosphere. Furthermore, P-lidars have proven to be valuable for the remote sensing of the Earth’s surface parameters, i.e., the surface texture and dielectric properties, which influence the multi-scattering processes and result in depolarization [41,57]. For example, P-lidars have the potential to provide information on soil, sand, and volcanic ash properties such as particle size and moisture content [58–60]; snow and ice characteristics such as age and types [61,62]; as well as plants and ground

cover such as types and classification [41]. In oceanic remote sensing, polarimetry has been a well-known tool in ocean optics. For example, with the elastic Mie backscattering, seawater’s optical properties can be estimated by retrieving the lidar attenuation coefficient over the laser penetrating depth [63]; with the depolarization effect of non-spherical particles, P-lidar can recognize ocean communities using the linear depolarization ratio [64,65]. Recent advancements have unveiled several promising applications in diverse fields, including the detection of oceanic scattering layers, fish schools, phytoplankton, seawater optical properties, and internal waves [66–70]. Figure 3 presents the triad of applications for P-lidar: (1) atmosphere remote sensing, which involves detecting clouds, precipitation, aerosol, and wind velocity; (2) oceanic remote sensing, such as phytoplankton layers’ detection, turbulence measurement, and fish school detection; (3) the remote sensing of the Earth’s surface, such as detecting and classifying vegetation, smoke, and urban objectives. From the figure, it is evident that P-lidar (as well as other lidar types) can be categorized into four groups: near-ground (terrestrial [71], ground-based [72], mobile [73], and UAV-based [74]), airborne [75], shipborne [76], and spaceborne/satellite-based lidar [77].

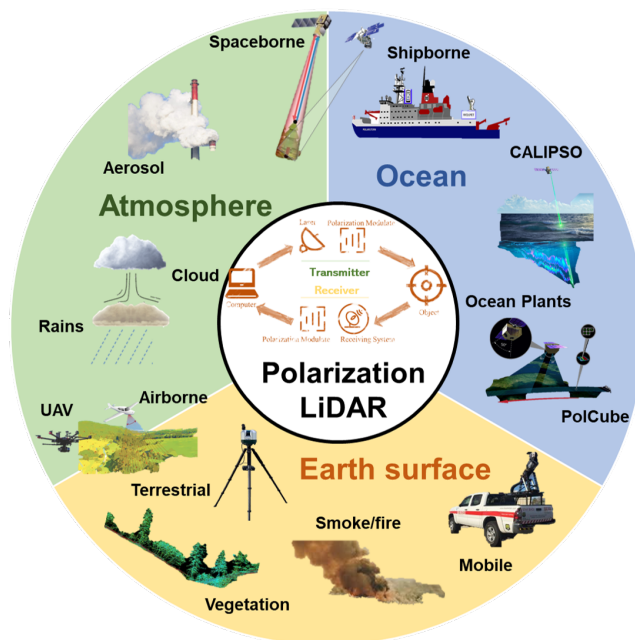


Figure 3. Triad of applications of P-lidar.

The rest of this review is organized as follows: Section 2 introduces the principles of polarization and lidar configurations. Section 3 surveys the representative applications of P-lidar in three fields, i.e., atmosphere, ocean, and the Earth’s surface. Finally, conclusions, a critical summary, and an outlook toward future research are presented in Section 4.

## 2. Principles of Polarization and P-Lidar

### 2.1. Polarized Light and Its Description

Currently, there are three main mathematical representations for polarized optics: Jones vector, Stokes vector, and Mueller matrix [1,2]; the first two are used to describe the polarization state of light, while the last one describes the polarization characterizes of materials or targets [78,79]. According to Maxwell’s electromagnetic theory, light propagates in space as a transverse wave, where the direction of the optical vector vibration is perpendicular to the direction of light propagation. Based on the theory of polarization, polarized light can be decomposed into two mutually orthogonal vectors,  $E_x$  and  $E_y$  [2].

The Jones vector (i.e.,  $\mathbf{J}$ ) describes both the amplitude and phase of the two orthogonal components, usually horizontal  $\mathbf{E}_x$  and vertical  $\mathbf{E}_y$ , of the electric field, as:

$$\mathbf{J} = \begin{bmatrix} \mathbf{E}_x \\ \mathbf{E}_y \end{bmatrix} = \begin{bmatrix} E_{0x}e^{j\delta_x} \\ E_{0y}e^{j\delta_y} \end{bmatrix}, \tag{1}$$

where  $(E_{0x}, E_{0y})$  and  $(\delta_x, \delta_y)$  denote the corresponding amplitudes and phases. If we use  $\mathbf{J}_i$  and  $\mathbf{J}_o$ , respectively, to represent the Jones vectors of the incident light and the out-going light after reflecting or scattering from a target, we can use a  $2 \times 2$  matrix  $\mathbb{J}$  (named the Jones matrix) to describe how the target changes the polarization of incident light, as:

$$\mathbf{J}_o = \mathbb{J} \mathbf{J}_i. \tag{2}$$

It is necessary to point out that the Jones matrix  $\mathbb{J}$  has four elements, all of which are complex numbers, which means it has a maximum of eight degrees of freedom [6].

Stokes first proposed a method in 1852 to represent arbitrary polarized light using four intensities, but he did not apply this method to the process of light scattering [80]. It was not until 1947 that Chandrasekhar utilized the Stokes vector to calculate the intensity vector of scattered light and represent the effects of polarization in the scattering process [2]. The Stokes vector, i.e.,  $\mathbf{S} = [s_0, s_1, s_2, s_3]^T$ , can be obtained from only power or intensity measurements and is sufficient to characterize the magnitude and relative phase, i.e., the polarization of a monochromatic electromagnetic wave [2]. The Stokes vector can also be written as a function of the polarization ellipse parameters: orientation angle  $\phi$ , ellipticity angle  $\chi$ , and ellipse magnitude  $A$ , as:

$$\mathbf{S} = \begin{bmatrix} E_{0x}^2 + E_{0y}^2 \\ E_{0x}^2 - E_{0y}^2 \\ 2E_{0x}E_{0y} \cos \delta \\ 2E_{0x}E_{0y} \sin \delta \end{bmatrix} = \begin{bmatrix} A^2 \\ A^2 \cos(2\phi) \cos(2\chi) \\ A^2 \sin(2\phi) \cos(2\chi) \\ A^2 \sin(2\chi) \end{bmatrix} \tag{3}$$

where  $\delta = \delta_x - \delta_y$ . From  $\mathbf{S}$ , one can obtain other polarization parameters. Three of them are the DoP (i.e.,  $P$ ), the degree of linear polarization (i.e., DoLP), and the degree of circle polarization (i.e., DoCP):

$$P = \frac{\sqrt{s_1^2 + s_2^2 + s_3^2}}{s_0}, \quad \text{DoLP} = \frac{\sqrt{s_1^2 + s_2^2}}{s_0}, \quad \text{DoCP} = \frac{s_3}{s_0}. \tag{4}$$

Obviously,  $P \in [0, 1]$ , and the light is non-polarized when  $P = 0$ ; completely polarized when  $P = 1$ ; and partially polarized when  $P \in (0, 1)$  [81]. It should be noted that one also defines the DoLP by the following Equation (5) when there only two orthogonal polarization components (i.e.,  $I_{\parallel}$  and  $I_{\perp}$ ) [81,82]. Another important parameter in the field of P-lidar is the depolarization ratio (i.e.,  $R$ ), which is also determined by  $I_{\parallel}$  and  $I_{\perp}$  [83,84].

$$\text{DoLP} = \frac{s_1}{s_0} = \frac{I_{\parallel} - I_{\perp}}{I_{\parallel} + I_{\perp}}, \quad R = \frac{I_{\perp}}{I_{\parallel}}. \tag{5}$$

Similar to the Jones vector and Jones matrix, the polarization characteristics of targeted objects can also be represented by corresponding matrices, connecting the incident and out-going light with Stokes vectors. The polarization states of the incident and out-going light are described by  $\mathbf{S}_i$  and  $\mathbf{S}_o$ , respectively [79]. Then, the polarization characteristics of the object can be represented by a  $4 \times 4$  Mueller matrix  $\mathbb{M}$ , as:

$$\mathbf{S}_o = \mathbb{M} \mathbf{S}_i. \tag{6}$$

Due to the fact that the elements of the Stokes vector are real numbers and have dimensions of intensity, the elements of the Mueller matrix  $\mathbb{M}$  are also real numbers and dimensionless. This is in contrast to the Jones vector and Jones matrix, which exhibit significant differences as they involve complex numbers and consider both amplitude and phase information [1]. The Mueller matrix solely represents the polarization characteristics of an optical element in terms of intensity transformations, without incorporating phase information [1]. The Jones matrix and the corresponding Mueller matrix can be connected by:

$$\mathbb{M} = \mathbb{C} \left( J \otimes J^* \right) \mathbb{C}^{-1}. \tag{7}$$

where  $\otimes$  denotes the Kronecker product,  $*$  represents the conjugation, and  $\mathbb{C}$  is

$$\mathbb{C} = \begin{pmatrix} 1 & 0 & 0 & 1 \\ 1 & 0 & 0 & -1 \\ 0 & 1 & 1 & 0 \\ 0 & i & -i & 0 \end{pmatrix} \tag{8}$$

Just as we claimed, both the Jones matrix and Mueller matrix are related to the ability of target objects to change the polarization state of incident light. In fact, when light interacts with targets, the polarization state can undergo the following changes: (1) alteration of the amplitude/intensity difference of the orthogonal polarization components; (2) modification of the phase difference between the two orthogonal polarization components; (3) changes in the direction of the two orthogonal optical fields. To characterize such changes, one can decompose, for example, the Mueller matrix into three different sub-matrices according to the Lu–Chipman decomposition method [85–87], as:

$$\mathbb{M} = \mathbb{M}_{dep} \cdot \mathbb{M}_{ret} \cdot \mathbb{M}_{dia}. \tag{9}$$

where the three sub-matrices represent the matrix related to depolarization, retardance, and diattenuation. The measurement of the Mueller matrix requires the establishment of at least 16 sets of intensity equations corresponding to different polarization states. This is because the Mueller matrix consists of 16 elements [1,88]. A typical Mueller measurement system includes two core modules: the polarization state generator (PSG) and the polarization state analyzer (PSA) [89,90]. The PSG and PSA are modulated four times each, resulting in a total of 16 intensity recordings, as:

$$\mathbb{I} = \mathbb{W}_{PSA} \cdot \mathbb{M} \cdot \mathbb{W}_{PSG}. \tag{10}$$

where  $\mathbb{W}_{PSG}$  and  $\mathbb{W}_{PSA}$  denote measurement matrices corresponding to the PSG and PSA, respectively. Then, by solving these equations, the Mueller matrix can be calculated, i.e.,

$$\mathbb{M} = \mathbb{W}_{PSA}^{-1} \cdot \mathbb{I} \cdot \mathbb{W}_{PSG}^{-1}. \tag{11}$$

More information about Mueller polarimeters can be found in previous publications [79,90].

### 2.2. Principle of P-Lidar

The lidar system is primarily divided into two parts: the signal-transmission system and the signal-receiving system [91–93]. At the transmission end of the lidar system, a pulse laser beam is emitted, interacting with the target object (such as particles in the air) through processes such as absorption, reflection, and scattering. The receiving system utilizes an optical telescope to receive the echo signals, which are then subjected to spectral analysis and opto-electronic conversion. Finally, through mathematical calculations and

inversion, various parameters of the target object with different meanings can be obtained. The lidar equation at a height/distance  $z$  is given by [94]:

$$P(z) = P_0 Y(z) \frac{ct_p}{2} \frac{Ar}{z^2} \beta(z) \exp \left[ -2 \int_0^z \alpha(z) dz \right] \tag{12}$$

where  $P(z)$  denotes the received power at height  $z$ ;  $P_0$  the peak power of the laser pulse;  $Y(z)$  the geometric overlap factor;  $c$  the speed of light;  $t_p$  the pulse width;  $Ar$  the receiving telescope area;  $\beta(z)$  the backscatter coefficient; and  $\alpha(z)$  the extinction coefficient [95,96].

P-lidar emits a polarized modulated (or unmodulated) beam at the laser-transmission end. Then, the beam interacts with the target object and is recorded at the receiving end through different polarization modulation techniques, such as a polarization beam splitter (PBS) [15,97]. The power of the echo signal corresponding to a special polarization component, for example at the polarization direction of  $\theta$ , can be obtained by:

$$P_\theta(z) = \frac{k_\theta P_0}{z^2} \beta_\theta(z) \exp \left[ -2 \int_0^z \alpha_\theta(z) dz \right] \tag{13}$$

where  $k_\theta$  denotes the system parameter at the state of polarization direction  $\theta$ , and can be considered as a constant. Based on the Mueller decomposition, Hayman et al. defined the Stokes vector lidar equation (SVLE) by linking the transmitted/received polarization states and the polarization properties of the target [47,48]. The equation is given by:

$$N(z) = \mathbf{o}^T \mathbb{M}_R \left[ \left( G(z) \frac{A}{R^2} \Delta z \right) \mathbb{T}(\mathbf{k}_b, z) \mathbb{F}(\mathbf{k}_i, \mathbf{k}_b, z) \mathbb{T}(\mathbf{k}_o, z) \mathbb{M}_T \mathbf{S}_L + \mathbf{S}_B \right] \tag{14}$$

where  $N(z)$  is the photon count vector for each polarization channel as a function of range  $z$ ;  $\mathbf{o}$  is the observation vector describing each polarization observation channel, each row of which is the polarization eigenvector related to each channel; and  $\mathbb{M}_T$  and  $\mathbb{M}_R$  are Mueller matrices related to the transmitter and receiver systems.  $G$  is the physical overlap function of the transmitter and receiver;  $A$  is the telescope area;  $R$  is the range resolution of the counting system;  $\mathbb{T}(\mathbf{k}_o, z)$  and  $\mathbb{T}(\mathbf{k}_b, z)$  are the out-going and back-going transmission Mueller matrices (wave direction vectors of  $\mathbf{k}_i$  and  $\mathbf{k}_b$ );  $\mathbb{F}$  is the phase matrix, which is a function of both transmitted and received wave vectors and range;  $\mathbf{S}_L$  denotes the Stokes vector of laser;  $\mathbf{S}_n$  denotes the Stokes vector of background noises.

Inspired by the formalism in Equation (10), we can simplify Equation (14) by using two generated measurement vectors ( $\mathbf{O}, \mathbf{B}$ ), as:

$$N(z) = \mathbf{B}^T \mathbb{F}(\mathbf{k}_o, \mathbf{k}_b, z) \mathbf{O} \tag{15}$$

where ( $\mathbf{O}, \mathbf{B}$ ), which are very similar to the measurement vectors related to the PSG and PSA part in a Mueller polarimeter, are determined by all the Mueller matrices on the way of out ( $\mathbf{O}$ )- and back-going ( $\mathbf{B}$ ):

$$\mathbf{O} = \mathbf{o}^T \mathbb{M}_R \mathbb{T}(\mathbf{k}_b, z), \quad \mathbf{B} = \mathbb{T}(\mathbf{k}_o, z) \mathbb{M}_T \mathbf{S}_L. \tag{16}$$

Based on the SVLE model, the basic principle of P-lidar is shown in Figure 4. All mathematical notations relevant to the model are, respectively, labeled at the transmitter and receiver locations to facilitate the readers' clear understanding of the model. Besides, in the configuration, the polarization modulation is optional, which depends on whether one needs a circular or linearly polarized beam in the P-lidar. The pulsed lasers generally used in lidar naturally produce linearly polarized light as the crystalline nature of the lasing media (e.g., a doped glass rod) and the method used in giant-pulsing, which typically relies on a polarization rotation device (e.g., a Pockels cell) to stop the cavity from lasing until the most-propitious instant. Sometimes, one may also use a cleaning polarizing sheet filter to

ensure the output beam’s polarization state [98]. Thus, basic P-lidar applications involve the transmission of a linearly polarized laser pulse [16].

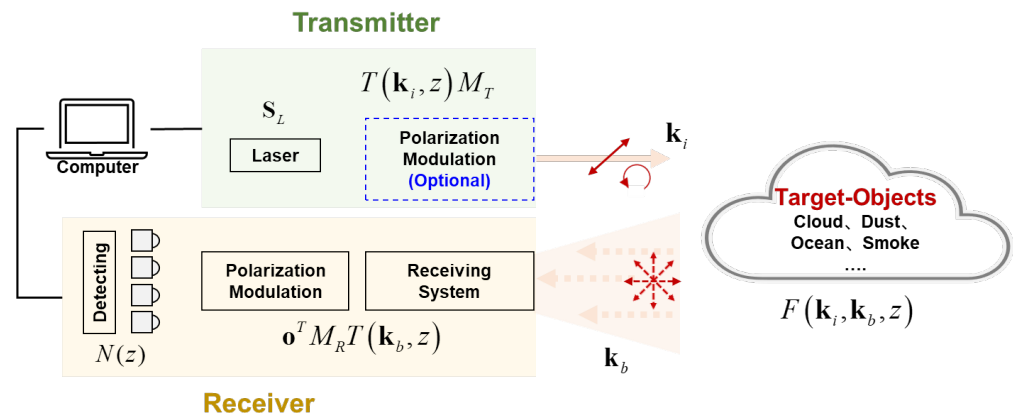


Figure 4. Principle of P-lidar.

According to the number of polarization modulation channels, which also is the number of detectors in the receiver, as shown in Figure 4, common P-lidars include dual-channel (2C), single-channel (1C), three-channel (3C), and four-channel (4C) configurations. Besides, if one wants to measure all elements in phase matrix  $\mathbb{F}$ , we need to obtain 16 measurements; in this case, we call it full P-lidar, and the receiver must have at least four channels, while the transmitter’s polarization modulation must include circularly polarized elements.

In the following, we will introduce the four types of P-lidar. However, it is important to note that the initial design of these four types was for single-point detection and cannot achieve two-dimensional or three-dimensional imaging. By adding a scanning module or an array imaging module to the system, lidar imaging can be achieved. Therefore, in the following, we also included an introduction to relevant imaging P-lidar systems.

### 2.2.1. Dual-Channel P-Lidar

The dual-channel configuration is the most-commonly used type of P-lidar. It can simultaneously measure the vertical polarization signal (i.e.,  $P_s$ ) and the parallel polarization (i.e.,  $P_p$ ) signal of the echo signal, providing real-time information about the depolarization ratio of the scattering medium [15,16,99]. Guasta et al. [44] from Italy were the first to propose the dual-channel P-lidar system, as shown in Figure 5.

The Cloud-Aerosol lidar with Orthogonal Polarization (CALIOP), which is carried by the CALIPSO satellite launched by NASA [99,100], is a typical dual-channel P-lidar. CALIOP has been in orbit and operating stably, providing abundant data for global atmospheric observations [101].

Although dual-channel P-lidar can provide real-time measurement of the vertical and parallel channel components of the echo signal and obtain depolarization ratio information, it is prone to misjudgment due to the influence of gain coefficients and system errors from various sources. As a result, there are many challenges in system calibration [102,103], and we will discuss the calibration process in the following Section 2.2.6.

### 2.2.2. Single-Channel P-Lidar

The main idea of single-channel P-lidar is to use the same detector to receive both the parallel polarization component and the vertical polarization component of the echo signal, thereby avoiding the need for gain ratio calibration. Figure 6 presents an example configuration of single-channel P-lidar.

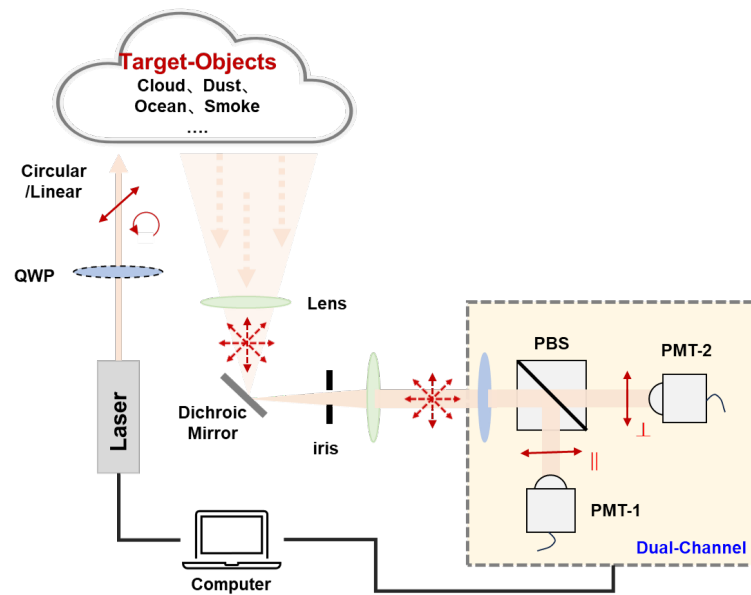


Figure 5. Examples of dual-channel P-lidar. PMT: photomultiplier, a detector.

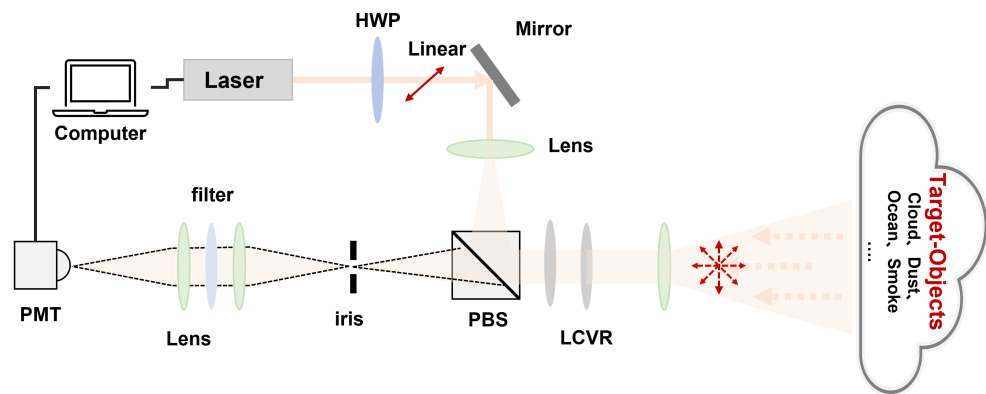


Figure 6. Examples of single-channel P-lidar.

In 1977, Plat et al. first proposed a single-channel P-lidar system, in which the transmitted laser polarization state remains unchanged, while the polarization direction of the analyzer in the receiving optical path rotates around the central optical axis by  $90^\circ$  with a rotation frequency consistent with the transmitted laser’s pulse repetition frequency [40,104]. As a result, the parallel polarization component and the vertical polarization component in the echo signal are sequentially received by the same detector, resolving the issue of system errors caused by gain coefficient influence.

However, the single-channel solution also has inherent issues. For dual-channel P-lidar, the parallel and vertical polarization components of the echo signal at any altitude are always synchronously received by two detectors, resulting in a depolarization ratio profile for each laser pulse. However, in the single-channel one, the detector can only receive the parallel polarization component of each laser pulse’s echo signal. It requires the combination of the echo signals from two consecutive laser pulses (with a time delay) to obtain a depolarization ratio profile, making the detection results highly susceptible to environment changes [105].

To address the real-time issue of single-channel solutions, Xia et al. in 2017 developed a new single-channel P-lidar based on a single-photon detector [50]. They utilized a polarization-maintaining fiber to receive the reflection signal from the PBS, reducing the time difference ( $40.6 \mu\text{s}$ ) for the signal to reach the detectors in the reflection and transmission channels. This allowed them to obtain real-time depolarization ratio profiles using a

single detector. However, this single-mode polarization-maintaining fiber is relatively long (8 km) and introduces an additional energy loss of approximately 30%.

### 2.2.3. Three/Four-Channel P-Lidar

The two types of P-lidar mentioned above are based on the parallel and vertical components of the echo signal. However, when the reflection or scattering from the target objects becomes more complex, errors can occur in depolarization analysis based on orthogonal polarization states. This can also be seen from the definition of the DoP, as shown in Equations (4) and (5), which state that the depolarization ratio (i.e.,  $R$ ) calculated based on orthogonal polarization components is just a simplified version of DoLP. Taking this into consideration and to further study the influence of multiple scattering on polarization changes, Pal et al. proposed a three-channel P-lidar [106]. At the receiving end, three telescopes are used to receive the signals, and polarization plates are used to modulate each beam channel with polarization directions of  $\parallel$ ,  $\perp$ , and  $45^\circ$ , respectively, to obtain the first three parameters of the Stokes vector, i.e.,  $s_0, s_1$ , and  $s_2$ , by

$$\begin{cases} s_0(z) = P_{\parallel}(z) + P_{\perp}(z) \\ s_1(z) = P_{\parallel}(z) - P_{\perp}(z) \\ s_2(z) = 2P_{45}(z) - s_0(z) \end{cases}, \tag{17}$$

Furthermore, based on Equation (3), angle  $\phi$  and ellipticity angle  $\chi$  can also be calculated, which provides more comprehensive information about the polarization characteristics of the measured object.

Three-channel P-lidar has primarily employed only a portion of the polarization information available by utilizing linear depolarization as the main observable. To extract more polarization information, the full Stokes vector has been studied, i.e., four independent measurements for  $s_0, s_1, s_2$ , and  $s_3$ . Houston et al. [107] designed a four-channel P-lidar, where the first receiver channel was used with its polarizer aligned parallel to the direction of linear polarization of the transmitted signal and the second with its polarizer aligned perpendicular to that of the transmitted signal. The third channel was set with its polarizer at an angle of  $45^\circ$  to this direction. In the fourth channel, the QWP reference axis was aligned with the transmitted polarization direction and the polarizer transmission axis at  $45^\circ$ . The recording four powers/intensities are denoted as  $P_{\parallel}(z), P_{\perp}(z), P_{45}(z)$ , and  $P_{circle}(z)$ , and the four Stokes parameters can be solved by:

$$\begin{cases} s_0(z) = P_{\parallel}(z) + P_{\perp}(z) \\ s_1(z) = P_{\parallel}(z) - P_{\perp}(z) \\ s_2(z) = 2P_{45}(z) - s_0(z) \\ s_3(z) = 2P_{circle}(z) - s_0(z) \end{cases}, \tag{18}$$

However, Houston et al. stated that the two-channel configuration for measuring  $R$  seems to be more efficient when compared to the four-channel configuration. This is because there is no significant additional information gained, but it does require additional instrumentation and data handling for the full four-channel measurements, at least for the examples presented in this work [107]. Of course, they also mentioned that further studies using a four-channel configuration are necessary to address certain issues and provide answers to specific questions.

In fact, the studies for three- and four-channel P-lidar have never stopped. The Clouds Aerosol Polarization and Backscatter Lidar (CAPABL) has been updated to include four on-orthogonal receiver polarization channels. These polarizations are all linear, i.e.,  $0^\circ, 90^\circ, 30^\circ$ , and  $110^\circ$ . It should be noted that this design does not aim to measure the full Stokes vector, but to provide more inversion methods, granting flexibility to optimize the polarization measurements [51].

### 2.2.4. Full P-Lidar

As we mentioned in the above section, to measure the polarization characteristics, denoted as  $\mathbb{F}$ , of a target object (such as scattered particles in the atmosphere), at least 16 detection signals are required. Additionally, the out-going light needs four linearly independent polarization states. The telescope's receiving system needs to simultaneously measure  $\mathbb{S}$  (which means at least four channels are necessary). In this configuration, both the transmitting end and the receiving end require a rotatable retarder. By continuously changing the polarization state of the transmitted laser and altering the polarization state of the received light path, multiple equations can be established to solve  $\mathbb{F}$ .

In 2004, Kaul et al. first proposed the use of a full-polarization lidar to detect and compute the atmospheric backscattering Mueller matrix [43]. In 2012, the Atmospheric Research Center in the United States retrofitted an existing high-spectral-resolution lidar, as shown in Figure 7 [48]. A QWP was rotated at the receiving end to generate circularly polarized light, obtaining the full Stokes vector and providing a comprehensive characterization of raindrop evaporation, condensation, and liquid water content.

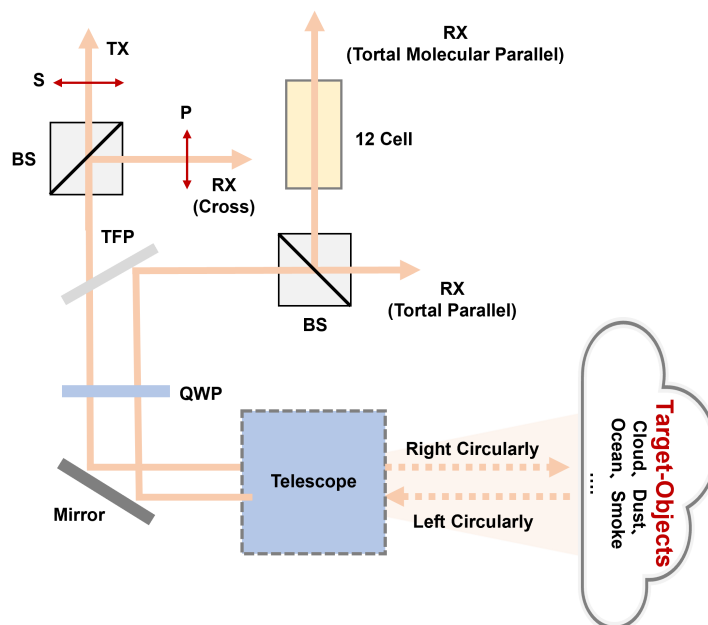
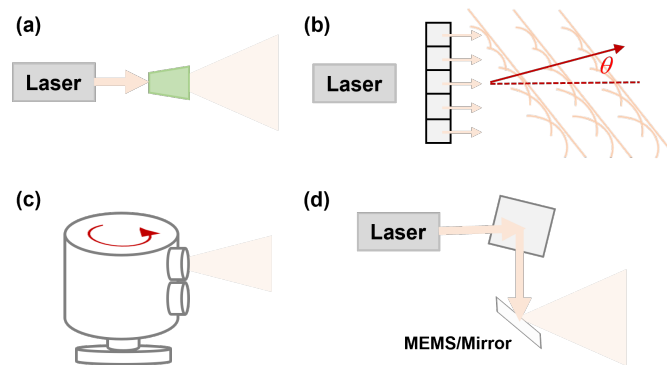


Figure 7. Examples of full P-lidar.

### 2.2.5. Scanning and Imaging P-Lidar Systems

The P-lidar systems introduced above do not incorporate scanning or mechanical motion devices, so they can only acquire point- or line-polarization information; we also call them non-scanning lidar or flash lidar [37]. In contrast, scanning P-lidar systems steer the laser beam and are more popular and mature as the captured data can reveal more diverse and complex polarization information of the target under test, such as information related to its direction or shape [108,109]. The simplest way to achieve this is to fix the transmitter or receiver ends of the above-mentioned system on a platform capable of mechanical motion or scanning [52,110]. Alternatively, scanning of the emitted beam can be achieved by adding a scanning mirror (or MEMS) at the transmitter end (for 2D scanning with a one-dimensional mirror or using a two-dimensional mirror for 3D scanning [111]). Generally, there are two classes of laser beam scanning: non-mechanical scanning and mechanical scanning. The former is also called solid-state beam scanning because it has no moving parts. We present these lidar types, i.e., non-scanning, optical-phased-array-scanner-based, motorized-spinning-scanner-based, and MEMS-/mirror-scanner-based, in Figure 8 to aid the readers' understanding, and more details can be found in [37,112].



**Figure 8.** Different types of lidar. (a) Non-scanning; (b) optical phased array scanner; (c) motorized spinning scanner; (d) microelectromechanical systems (MEMS)/mirror laser scanner.

LOSA-M3, developed at the V. E. Zuev Institute of Atmospheric Optics, the Siberian Branch of the Russian Academy of Sciences, is a scanning P-lidar [52]. As depicted in Figure 9, it is equipped with an automatic scanning device that allows for changing the sensing direction in the upper hemisphere at speeds of up to  $1.5^\circ \text{ s}^{-1}$  with an angle measurement accuracy setting of at least 1 arcmin. Bissonnette et al. chose to perform the scanning by rotating a mirror mounted at  $45^\circ$  to the laser axis, with a speed of  $3.5^\circ \text{ s}^{-1}$ , and its rotation axis is the same as the transceiver axis. However, it should be noted that, for an accurate assessment of measurement errors, it is necessary to measure the refractive index of the applied mirror coating with good accuracy [113]. To some extent, the process of acquiring data using scanning P-lidar is imaging. One can also use imaging sensors (traditional imaging CCD, electron multiplying CCD, or polarization camera), instead of PMT in non-scanning P-lidar, to achieve polarization-sensitive imaging lidar [54,55,114].

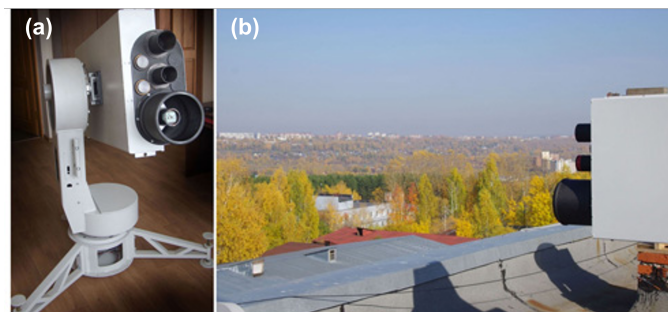


**Figure 9.** Photographs of the scanning polarizing lidar LOSA-M3 on a rotary column in the laboratory room (a) and on the roof of the institute’s building (b) [52].

### 2.2.6. Calibration for P-Lidar Systems

In fact, achieving high-precision depolarization ratio measurements is crucial for subsequent applications and has been a focal point of P-lidar [115]. The main error sources for the depolarization ratio include the calibration error of the gain ratio, the error caused by impurities in the transmitted laser’s polarization state, the alignment error between the laser polarization vector and the incident plane of the PBS, and the polarization crosstalk caused by the inability of the PBS to achieve 100% reflection and transmission [103,116,117]. Among these errors, the calibration error of the gain ratio (the first one) plays a decisive role in determining the final measurement accuracy; as a result, various methods for calibrating the gain ratio are continuously being proposed.

The most-common calibration methods are the  $+45^\circ$  method, the  $\Delta 90^\circ$  method, the  $\Delta 45^\circ$  method, the rotation-fitting method, and the pseudo-depolarizer method. For example, CALIOP used the pseudo-depolarizer method to calibrate the gain ratio of the system [118], while the Multichannel Lidar System (MULIS) and Portable Lidar System (POLIS) used the  $\Delta 90^\circ$  method [119]. Liu et al. from Zhejiang University systematically

compared the accuracy and pros and cons of the four methods under different alignment angle conditions for gain ratio calibration [120]. Through theoretical and experimental comparisons, they provided the best choice for gain ratio calibration methods. The  $+45^\circ$  method's advantage lies in its simple operation, but its drawback is that it neglects the effects of alignment angle errors and polarization crosstalk, which may introduce errors [121]. The  $\Delta 90^\circ$  method is relatively easy to operate and provides higher accuracy, but it cannot eliminate alignment angle errors [98,122]. The  $\Delta 45^\circ$  method improves calibration speed while ensuring calibration accuracy, but its drawback is that it cannot exclude the influence of atmospheric state changes [116]. The rotation fitting method's advantage is that it can simultaneously invert three unknowns, namely the gain ratio, depolarization ratio, and initial alignment angle, without requiring prior knowledge. However, its drawbacks are that calibration takes a longer time, the operation is cumbersome, and it is only suitable for relatively stable atmospheric environments [103]. The depolarizer method is advantageous for its simplicity and real-time calibration, which eliminates the influence of atmospheric environment changes. However, the commercial depolarizer may still have difficulties generating completely depolarized light, introducing other errors [117,118].

### 3. Applications

#### 3.1. Atmospheric Remote Sensing

Lidar and polarimeter technologies complement each other effectively. Lidar excels at detailing aerosol profiles and types, while polarimeters offer constraints on overall aerosol abundance, absorption, and microphysical properties [13,101]. Combining these methods enhances aerosol property observations; this is also why P-lidar has been widely employed in atmospheric remote sensing to study the optical properties of the atmosphere and the characteristics of particles such as aerosols, clouds, and water vapor. Specifically, P-lidar can measure the polarization scattering characteristics of aerosol particles, providing information about aerosol concentration, size distribution, shape, etc. This is crucial for understanding aerosol sources, transport, and interaction mechanisms in the atmosphere. By measuring polarization scattering properties using P-lidar, information such as aerosol types, cloud optical thickness, particle size, and shape distribution can be obtained.

This is significant for studying cloud formation and evolution and their impact on climate and weather. P-lidar can measure atmospheric transparency parameters such as atmospheric optical thickness and aerosol optical depth. This is important for monitoring atmospheric pollution and studying atmospheric composition [14,49].

In 1963, the Massachusetts Institute of Technology (MIT) established the first lidar based on ruby lasers, which was used to detect high-altitude aerosols in the troposphere and middle atmosphere [123]. This marked the beginning of the development and application of lidar for aerosol detection. Around the same time, mature polarization optical techniques were applied to lidar systems. In the 1960s, New York University began using polarization lidar, i.e., P-lidar, systems to observe atmospheric ice crystals and water droplets [39]. As shown in Figure 10, ice crystal detection hinges on measuring the volume depolarization ratio. While backscattering from spherical objects (such as liquid drops) at exactly  $180^\circ$  yields no depolarization, non-spherical crystal backscattering introduces notable depolarization through multiple internal reflections. Thus, the volume depolarization ratio effectively distinguishes between cloud layers with water drops and those where backscattering by ice crystals prevails [124]. In 1971, Schotland et al. conducted research on the depolarization ratio of water vapor condensates [39]. Understanding and quantifying the various forms of ice crystals in the atmosphere and precipitation are crucial for comprehending microphysical and radiative processes in different scenarios and improving regional and global climate models. In 2017, Sergey et al. used measurements from the U.S. Department of Energy's Atmospheric Radiation Measurement (ARM) program's cloud P-lidar to retrieve the nonsphericity of ice particles. The observed ice particles included irregularly shaped crystals and aggregates, with aspect ratios spanning from around 0.3 to 0.8 [125].

Using polarization information for particle shape measurement and properties' analysis is a well-established technique. In 2015, Wu et al. developed the Water Vapor, Cloud, and Aerosol Lidar (WACAL) for comprehensive atmospheric measurements, including the water vapor mixing ratio, depolarization ratio, backscatter and extinction coefficients, and cloud information [126]. The WACAL system, featuring Raman, polarization, and infrared channels, was installed at Qingdao Ocean University, enabling the assessment of aerosol and cloud optical properties and water vapor mixing ratios. In 2019, Tan et al. introduced a novel method to infer the phase state of submicron particles using linear depolarization ratios obtained from P-lidar [127]. This innovative approach demonstrated the feasibility of inferring aerosol phase distributions and established a parameterization scheme for deducing aerosol phase states from backscatter depolarization ratios, marking a significant advancement in real-time aerosol phase state profiling. In 2020, Jimenez et al. first introduced a novel cloud-retrieval technique using lidar observations of the volume linear depolarization ratio at two different receiver field of views (FOVs) to retrieve the micro-physical properties of liquid cloud layers [128] and then applied it to cloud measurements in pristine marine conditions at Punta Arenas in southern Chile [129]. Following Jimenez's work, in 2023, Zhang et al. introduced a dual-FOV high-spectral-resolution Lidar (HSRL) for simultaneous analysis of aerosol and water cloud properties, particularly the microphysical properties of liquid water clouds. This instrument allowed for continuous monitoring of aerosols and clouds and underwent validation through synchronous observations, including Monte Carlo simulations and other methods, to investigate the interplay between aerosol levels and the microphysical properties of liquid water clouds [130].

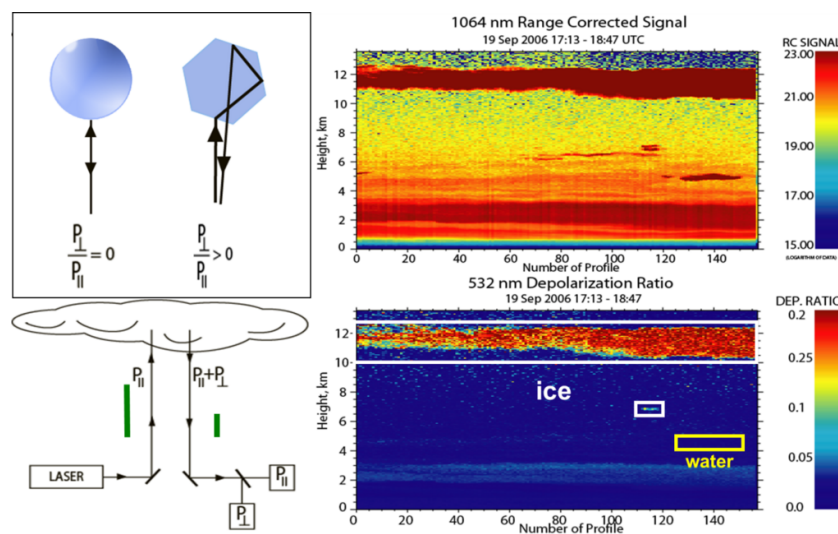


**Figure 10.** Demonstration of P-lidar for distinguishing liquid cloud droplets and ice crystals [124].

Another important application, aside from distinguishing various aerosols' shapes, is the identification of different types/altitudes of clouds. In 1977, Pal and Carswell utilized ruby lasers at 347 nm and 694 nm wavelengths as fundamental and second harmonic laser sources, respectively, to measure the depolarization ratio of falling snow, ice crystals, cumulonimbus clouds, and low-level rain clouds [61,131]. Their findings indicated a positive correlation between the depolarization ratio and cloud height, with clouds exhibiting a higher depolarization effect on 347 nm laser light compared to 694 nm laser light. In 1991, Sassen conducted research on the polarization characteristics of various cloud types using a P-lidar. He observed depolarization ratios of less than 0.15 for liquid water clouds, around 0.50 for cirrus clouds, and values between these two for mixed clouds [15,132]. P-lidars can be also applied to separate the dust and non-dust (e.g., the smoke) parts [133–135]. For example, Sugimoto et al. used the depolarization ratio and the volume backscatter coefficient (both at 532 nm and 1064 nm) to retrieve the dust and non-dust and the spectral dependence of the backscatter-related Ångström exponent [136,137]. By combining the

multi-wavelength Raman lidar and P-lidar, Tesche et al. separated the optical properties of desert dust and biomass burning particles by using the depolarization ratio [138].

The advantages of P-lidar in detecting optical and microphysical properties of aerosol particles can also be extended to aerosol classification as different aerosols exhibit varying responses to different optical wavelengths. Among these different choices of optical wavelength, the 355 nm and 532 nm wavelengths are the most-widely used combinations. In 2014, Huang et al. developed a dual-polarization lidar system that simultaneously measured polarization at 355 nm and 532 nm wavelengths. During observations of dust and haze events in northern China, it was found that dust-dominated aerosols exhibited a higher depolarization ratio at 532 nm compared to 355 nm, whereas air pollutants showed relatively low depolarization ratios. This suggests that such multi-wavelength systems have the potential to enhance aerosol classification accuracy [49]. In 2021, Qi et al. developed a ground-based dual-polarization lidar system capable of simultaneously measuring polarization at 355 nm and 532 nm wavelengths to identify aerosol and cloud types [53]. Their findings revealed significant differences in volume depolarization ratios between typical aerosols and cloud layers at the two wavelengths. In addition to the above two wavelengths, the depolarization ratio measurement at 1064 nm is also useful. More details about its applications can be found in previous references [139–141].

In 2021, Kong et al. introduced a P-lidar system designed for precise all-weather retrieval of atmospheric depolarization ratios. This system simultaneously captured four-directional P-lidar signals, offering numerous possibilities for real-time field measurements of dust, clouds, and urban aerosols, directional particles (another typical work is [142]). Furthermore, the team employed laser diodes and a polarization camera to create a visible and near-infrared dual-polarization lidar technology for unattended atmospheric aerosol field measurements in all-weather conditions. Using one month of continuous atmospheric observation data, they analyzed and assessed the spectral features, including the aerosol extinction coefficient and the linear particle depolarization ratio (LPDR). Through this analysis, different types of aerosols were able to be classified [55].

There are three primary methods for detecting atmospheric aerosols: ground-based observations, airborne, and satellite remote sensing. Among these, using a lidar on moving platforms such as aircraft or satellites is the most-effective way to gather regional-scale aerosol data. In 2006, CALIPSO, a spaceborne P-lidar, successfully launched, equipped with a dual-wavelength (532/1064 nm) laser and a three-channel (532 nm P/S channels and 1064 nm) receiver. CALIPSO identifies clouds, measures particle content, and creates atmospheric profiles for research purposes. It is employed to detect the vertical distribution of aerosols and clouds, ascertain the cloud particle phase (via the signal ratio at 532 nm in parallel and perpendicular polarization channels), and classify aerosol sizes using the wavelength-dependent backscatter-related Ångström exponent [45,143].

Recently, MIT has been designing a satellite-based P-lidar system to categorize aerosols, as shown in Figure 11a. The system comprises two satellites: the primary satellite emits polarized laser pulses, while the second satellite is equipped with a lidar receiver that captures images of scattered polarization [144]. The proposed architecture enhances a satellite-based lidar system by introducing a second lidar receiver satellite, flying in formation with the transmitting satellite, to capture obliquely scattered light. The primary satellite emits polarized laser pulses, and the secondary satellite generates polarization-analyzed lidar images of the illuminated atmospheric column. Due to its oblique perspective, the secondary satellite observes changes in polarization that are not accessible to the primary satellite. These polarization variations provide critical information for aerosol classification.

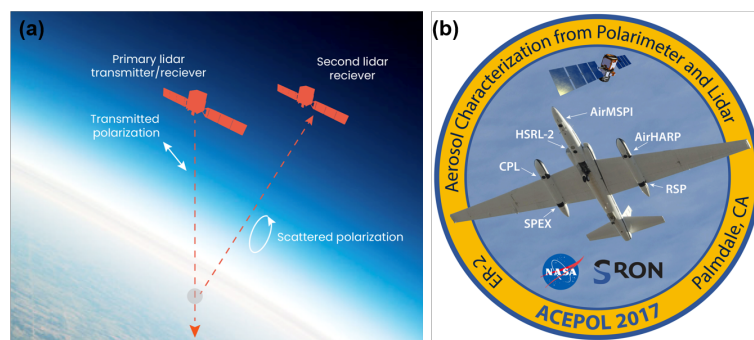


**Figure 11.** (a) P-lidar system with two satellites [144]. (b) The ACEPOL field campaign emblem [145].

Airborne lidar provides mobility and a high signal-to-noise ratio (SNR), serving as a valuable complement to spaceborne lidar. In 2003, Dulac et al. utilized the airborne P-lidar known as ALEX to study multi-layer aerosol structures in the Eastern Mediterranean [146]. In 2012, Bo et al. developed an all-weather atmospheric aerosol–water vapor lidar system for aircraft. This system simultaneously captures backscatter at 355 nm/532 nm wavelengths, 532 nm depolarization, and nitrogen and water vapor molecular Raman signals, facilitating long-term monitoring of aerosols and water vapor [147]. Another famous airborne system is the Aerosol Characterization from Polarimeter and Lidar (ACEPOL), which was conducted in the fall of 2017 by NASA. Figure 11b shows the ACEPOL emblem, which illustrates the locations of the remote sensing instruments on the aircraft, with two on the fuselage and two in each wing pod [145]. Additionally, there is a growing emphasis on developing portable P-lidar systems. For instance in 2021, Kong et al. introduced a portable P-lidar system using a focal-plane-splitting scheme. This system is designed in a T-shaped structure, featuring a sealed transmitter and a detachable large-aperture receiver. It is well-suited for cost-effective, low-maintenance outdoor unmanned measurements [13].

As detection instruments continue to progress, research algorithms are also undergoing gradual evolution. Many solutions to the lidar equation for elastic scattering (e.g., Fernald et al. [148], Klett [149], Davis [150], Sasano and Nakane [151], and Collis and Russell [152]) have been proposed. Among these solutions, the Fernald analysis method treats atmospheric molecules and aerosol particles separately, making it the current pinnacle of inversion methods under development [153]. Building upon Fernald's forward inversion technique, CALIOP employs the hybrid extinction retrieval algorithm (HERA), known for its flexibility and robustness as an iterative inversion method [99]. It utilizes hierarchical position data from the selective iterative boundary locator (SIBYL) and layer classification results from the scene classification algorithms (SCAs) to determine particle backscatter and extinction coefficients. It should be noted that Raman and HSRL, as the two typical systems to provide high-quality backscatter and extinction coefficients, have the potential for providing vertically resolved information about aerosol size/concentration [154,155]. For example, Thorsen et al. developed a comprehensive set of algorithms for processing the Raman lidar data to obtain the retrievals of aerosol extinction and feature detection. The details of the Raman algorithms for aerosol backscattering and extinction can be found in [156,157]. The HSRL data were processed in a manner akin to that of the Raman lidar data, ensuring alignment in terms of timestamps, altitudes, as well as temporal and vertical resolutions. While it is worth noting that the HSRL does not employ distinct low- and high-sensitivity channels, the processing and averaging approach for HSRL data is to mimic the processing of the Raman lidar low- and high-sensitivity channels for consistency. In 2017, based on the above algorithms, Ferrare et al. processed both the Raman lidar and HSRL to obtain a consistent set of profiles, with equivalent resolutions and averaging, across all wavelengths [158]. Recently, there have also been many researchers focused on developing advanced algorithms. For example, in 2022, the researchers in Italy employed a Bayesian parameter approach to infer the atmospheric particle size distribution [159]. In April of the same year, based on the spaceborne Aerosol and Cloud High-Spectral-Resolution Li-

dar (ACHSRL), capable of highly precise global aerosol and cloud detection, launched by China, Ju et al. proposed a retrieval algorithm for deriving aerosol and cloud optical properties from ACHSRL data, comparing it against end-to-end Monte Carlo simulations for validation. These efforts involved the use of the airborne prototype of ACHSRL [160].

### 3.2. Remote Sensing of Earth's Surface

In applications related to terrain characterization, vegetation remote sensing, and other surface environmental studies, microwave radar has been proven to possess certain advantages. However, due to its relatively long wavelengths, it cannot provide high-resolution information about targets. Lidar, on the other hand, operates at shorter wavelengths, enabling sufficient resolution of surface environmental structures and, thus, enhancing the performance of relevant applications.

In vegetation remote sensing, traditional lidars are mainly used for measuring height and echo intensity, thus inferring the three-dimensional surface structure of vegetation. One example is the Scanning lidar Imager of Canopies by Echo Recovery (SLICER) scanning lidar system [161]. SLICER used a 1064 nm neodymium-doped yttrium aluminum garnet (Nd:YAG) laser with a beam divergence angle of approximately 2 mrad. Under normal operating conditions, SLICER had a footprint diameter of about 9 m, and it could obtain the canopy height, above-ground biomass, cross-sectional area, and other forest characteristics. Another example is the vegetation canopy lidar, a spaceborne lidar system with three 1064 nm Nd:YAG lasers, providing a 25 m field of view at an altitude of 400 km. It can characterize the three-dimensional structure of the Earth's surface on a global scale and offer improved global forest canopy height detection and biomass estimation [162]. However, all these lidars are non-polarimetric, and the ability to study the polarimetric properties of vegetation is of great significance.

In 1993, the NASA Goddard Space Flight Center made the first airborne laser polarization sensor (ALPS), i.e., a P-lidar, for the remote sensing of the Earth's surface (vegetation) [41]. ALPS has a linearly polarized Nd:YAG laser source at both 1064 and 532 nm, with a detector field of view of approximately 0.03 rad. It can measure desired parameters such as the total backscatter and the polarization state. Using the ALPS system, researchers were able to distinguish unique cross-polarization signatures for different tree species, such as broadleaf and coniferous trees [41]. This system also revealed a significant correlation between near-infrared depolarization and crop parameters, specifically nitrogen fertilization. The depolarization spectral difference index proved to be effective for estimating crop yields [163]. However, one limitation of the ALPS system was its inability to capture the lidar return waveform, which prevented obtaining detailed information about the vertical structure of the vegetation canopy. To handle this issue, the University of Nebraska has refurbished the ALPS system and developed it into a multi-wavelength airborne P-lidar system, named MAPL [164]. MAPL's receiver has four channels (dual-wavelength and dual-polarization detection) and records the entire lidar waveform. Therefore, it can study both vegetation canopy structure and the characterization of vegetation cross-polarization [165]. The same team also used MAPL to study the polarimetric reflectance from different tree species in the forest and proved its ability to detect different trees by analyzing the lidar waveform shapes, the depolarization ratios, and the reflectance percentages [166]. In 2018, Tian et al. proposed the measurement of co-polarized and cross-polarized components of maize leaves at a 532 nm laser wavelength [167]. They analyzed the depolarization differences under varying biochar contents and demonstrated that the laser depolarization ratio could serve as an indicator to monitor plant growth conditions.

P-lidars can also be applied for forest fire/smoke detection. By detecting and analyzing the backscattering process caused by the interaction between atmospheric particles and lasers, lidar can achieve precise measurements of smoke. However, traditional intensity-based lidar needs to find a commanding height for scanning, which is often hard to fulfill [168,169]. Moreover, due to the complexity of forest terrains, as they contain leaves and other obstacles, the lidar signals must pass through these leaves and obstacles, which

makes it difficult to distinguish forest-fire smoke with a single-channel lidar. To solve this problem, Xian et al., in 2020, proposed a scanning P-lidar system to detect smoke from forest fires [108]. This system uses a 1064 nm pulsed laser and differentiates smoke from lidar signals contaminated by forest obstacles through the depolarization ratio.

A very important function of scanning or imaging lidar is its ability of 3D imaging in Urban remote sensing. The first polarization-modulated 3D lidar was proposed by Taboada and Tamburino in 1992 [170]. In order to improve the image quality, Chen et al. proposed an electron-multiplying charge-coupled-devices (EMCCDs)-based lidar system, in which the echo signal is separated into two orthogonal polarized components via a PBS. Such a polarization-modulated method improves the range accuracy of the objects of interest from 4.4 to 0.26 m with a gate opening range of 200 m [171]. In 2018, the same team found that the 3D imaging P-lidar had very promising performance in an FOV of 0.9 mrad [172]. The mentioned types of P-lidar, to some extent, belong to dual-channel P-lidar because they can only simultaneously acquire orthogonal polarization states. However, these systems require two cameras and a PBS to obtain orthogonal polarization states, making pixel-level alignment challenging [173]. In 2016, Jo et al. proposed a 3D flash P-lidar based on a micro-polarizer camera, as shown in Figure 12a, which can obtain the linear Stokes vector with a single shot [174], and achieved a spatial resolution and range precision of 0.12 mrad and 5.2 mm at 16 m, respectively [175].

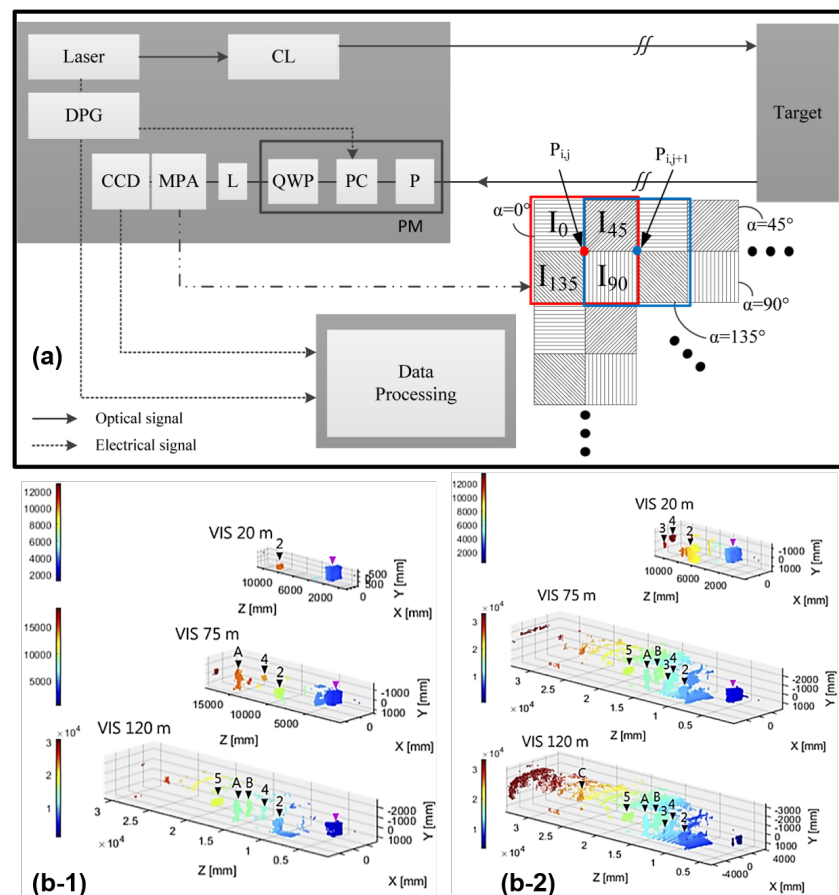


**Figure 12.** (a) P-lidar based on a polarization camera [175]. (b) Reconstructed point clouds for (b-1) co-polarization and (b-2) cross-polarization configurations at 20 m, 75 m, and 120 m of visibility [7].

Another important application is autonomous driving, as lidar sensors are one of the key supporting technologies for implementing autonomous driving. Nunes-Pereira et al. demonstrated through experiments that the reflection signals from metallic car paints have distinct polarization characteristics [176]. Therefore, by using a P-lidar, distance measure-

ments can be supplemented, thereby aiding in target classification. In their experiments, they utilized a custom-built P-lidar system, which employed a pulsed, linearly polarized 785 nm laser, a pair of 2D scanning galvanometer mirrors, and a linear polarizer positioned in front of the collection objective. The polarizer was alternately set for co-linear and cross-linear polarized detection. Including polarization into the lidar can improve autonomous driving performance in a dense atmosphere. In 2021, Ronen et al. introduced a model that combines traditional lidar and Stokes–Mueller formulations and conducted experiments inside an aerosol chamber [177]. The results showed that the use of a polarized source together with a cross-polarized receiver can improve the target-signal-to-atmospheric-signal ratio in a dense aerosol medium for a lidar system. Therefore, implementing polarimetric imaging techniques in lidars can enhance the performance of autonomous vehicles in poor-visibility conditions. Actually, this characteristic of polarization information can be found in many applications of polarization imaging [5,6]. In 2022, Ballesta-Garcia et al. studied the performance of P-lidar in a macro-scale fog chamber under controlled fog conditions and demonstrated many interesting findings [7]. For example, a system based on circularly polarized incident light and cross-polarized configuration helps to reduce the SNR, and a cross-polarized configuration enables the detection of objects while allowing the filtering out of most of the fog response, as shown in Figure 12b.

### 3.3. Ocean Remote Sensing

Aerosol observations utilize various passive and active remote sensing techniques, which can be applied to the ocean to better characterize hydrosols and enhance the atmospheric-correction process. While spectral radiance provides sensitivity to the absorption and scattering properties of constituents within the water column, polarized light emerging from the Earth system carries a wealth of information about the atmosphere, ocean, and surface, which remains underutilized in ocean color remote sensing. Polarized light originating beneath the ocean surface contains valuable microphysical details about hydrosols, including their shape, composition, and attenuation. Retrieving such information is challenging, if not impossible, using traditional scalar remote sensing methods alone. Moreover, polarimetric measurements offer opportunities to enhance the characterization and removal of atmospheric and surface reflectance that can interfere with ocean color measurements.

Kattawar et al. [178] were pioneers in conducting vector radiative transfer simulations for a coupled atmosphere–ocean system. It was not until 30 years later, in 2006, that Chowdhary et al. [179] first introduced models specifically addressing the polarized contribution from the ocean for photopolarimetric remote sensing observations of aerosols above the ocean [180]. This marked the beginning of increased interest in ocean-related applications of polarimetry. In 2007, Chami demonstrated the potential advantages of utilizing polarimetry to understand the optical and microphysical properties of suspended oceanic particles (hydrosols) through radiative transfer (RT) simulations [181]. In aquatic environments characterized by the prevalence of phytoplankton, the polarized reflectance at the top of the atmosphere exhibits a high degree of insensitivity to fluctuations in chlorophyll concentration. In 2009, Tonizzo et al. [182] developed a hyperspectral, multiangular polarimeter designed to measure the polarized light field in the ocean, accompanied by an RT closure analysis, which validated the theoretical analysis. Additionally, in 2010, Voss and Souaidia successfully measured the upwelling hemispheric polarized radiance at various visible wavelengths, revealing the geometrical dependence of polarized light [183].

Oceanic lidars can penetrate seawater to acquire highly accurate vertical profiles of multiple parameters within the ocean. Since the introduction of the first bathymetry lidar in 1968, various types of ocean lidars have been developed to assess different oceanic parameters and constituents. In particular, P-lidar, widely employed in oceanic studies, offers significant advantages in providing multiple oceanic parameters. Analyzing the elastic Mie backscattering signal, seawater's optical properties can be estimated by retrieving the lidar attenuation coefficient within the laser's penetration depth. Additionally, it can identify

oceanic communities through the linear depolarization ratio, owing to the depolarization effect of non-spherical particles on incident light. In other words, oceanic P-lidar has achieved successful applications in various domains such as the retrieval of depolarization optical products in the upper ocean [67], the detection of phytoplankton layers [184,185], turbulence measurement [186,187], and marine biological population detection [188,189].

Over the past decade, oceanic P-lidar has found numerous applications in oceanographic research. For example, Vasilkov et al. employed an airborne P-lidar to generate profiles of the scattering coefficient and identified subsurface layers with high scattering properties during their field experiments [75]. Furthermore, Churnside et al. developed a radiative transfer equation for airborne polarized lidar returns, facilitating the detection of scattering layers, fish schools, seawater optical properties, and internal waves [67]. To expand the scope of ocean observing efforts, Collister et al. designed a shipborne lidar to investigate the combined impacts of particle composition and seawater multiple scattering based on the lidar's linear depolarization ratio [190]. Behrenfeld et al. quantified phytoplankton biomass and diel vertical migration using the particulate backscattering coefficient and diffuse attenuation coefficient derived from the spaceborne P-lidar CALIOP [64]. Chen et al. observed the vertical distribution of subsurface phytoplankton layers in the South China Sea using a dual-wavelength airborne P-lidar [70]. Furthermore, Chen et al. introduced the planned "Guanlan" ocean remote sensing mission, featuring a near-nadir-pointing oceanic lidar and a dual-frequency interferometric altimetry system [70]. The oceanic lidar payload is expected to contribute significantly to our understanding of the marine food chain and ecosystem by providing data with a 10 m vertical resolution within the euphotic layer, advancing our knowledge of both the dynamic and bio-optical characteristics of the oceanic mixed layer.

Marine biological population detection is also a promising application for oceanic lidars. Likely, the initial development of the theory for using lidar to detect fish schools was pioneered by Murphree et al. [191]. The first experimental trials, conducted in a controlled environment, were carried out by Swedish scientists [192]. In 1999, Churnside from the National Oceanic and Atmospheric Administration (NOAA) developed an airborne lidar for marine fisheries. This lidar is indeed a single-channel P-lidar and uses a polarizer in front of the telescope system to select either the component of the return that is co-polarized with the laser or the cross-polarized component [42]. Their results showed that one can see fish from an airborne P-lidar. In clear water, one can see to depths of 40–50 m, and in turbid waters, this depth penetration is reduced. In 2010, Churnside took a case study in Chesapeake Bay, by using the cross-polarized component as its contrast between fish, and the background-scattering level was greater than that of the co-polarized return. They found that the average depth penetration of lidar was 12 m, and the average depth of detected schools was 3 m [46]. In 2018, Shamanaev proposed a method of P-lidar sensing of marine fish schools based on a comparison of the numerical values of the lidar return power and depolarization with their threshold levels determined by the sea water extinction index in the fishery region [193].

Another example is jellyfish detection, which facilitates the acquisition of data encompassing jellyfish taxonomy, population metrics, spatial dispersion, and related particulars. This process holds a pivotal role within the ambit of jellyfish prevention and management. The existing methodologies for jellyfish detection presently exhibit limitations in terms of detection efficiency, precision, and vertical distribution insights. P-lidar holds the potential to accomplish remote sensing of individual jellyfish organisms. This advanced technology offers an efficient, cost-effective, and accurate means of monitoring variations in jellyfish distribution and population dynamics. Currently, there is a relatively limited amount of research focused on utilizing marine lidar for jellyfish detection. In 2015, Churnside et al. [189] employed an airborne polarized marine lidar to observe the phenomenon of hollow aggregations within jellyfish populations. Their findings were corroborated by sonar detection results, thereby substantiating the viability of using polarized marine lidar for jellyfish population detection. In August 2017, a shipborne polarimetric

marine lidar, independently developed by the research team at Zhejiang University, China, conducted experimental measurements in the Yellow Sea [194]. During these experiments, it observed a wealth of strong scattering signals. By combining these data with video monitoring information, the team was able to identify the source of these signals as jellyfish, demonstrating that jellyfish in the same area exhibited clustering patterns in their optical characteristics. Furthermore, jellyfish signals from different regions had similar contrast, but varied depolarization rates, suggesting that the optical properties of jellyfish are closely related to their local environmental conditions.

Besides, P-lidar can be used to detect sea surface oil spills. Oil spillage on the sea surface tends to create a film, impeding the exchange of gases between the sea and the atmosphere. This results in a reduction of dissolved oxygen in the seawater. Research has revealed that the complete oxidation of 1 kg of petroleum requires the consumption of approximately 400,000 L of dissolved oxygen from seawater. Consequently, oil spill pollution can lead to extensive areas of hypoxia [195]. During the 1990s, the University of Oldenburg (Germany) achieved a significant milestone by successfully developing a marine lidar system, which was subsequently employed for real-time monitoring of oil spill areas [196]. Furthermore, countries such as Canada, France, and Italy have also sequentially developed airborne lidar systems for oil spill monitoring [197]. In 2009, the marine fluorescence lidar system developed by Zhao et al. underwent multiple experiments in the vicinity of Qingdao. In 2021, the Aerospace Science and Technology Corporation's 9th Academy successfully completed emergency monitoring tasks for oil spill incidents in the Yellow Sea, utilizing unmanned aerial vehicles (UAVs) equipped with their self-developed dual-wavelength polarized marine-detection lidar, X-band target surveillance radar, and miniaturized synthetic aperture radar (MiniSAR) [198]. The results indicated that the P-lidar system exhibited reliable performance in monitoring oil spills on the sea surface. It could accurately differentiate the types of oil spills and assess the degree of oil pollution [199].

Previous studies predominantly used 532 nm lasers in oceanic P-lidar due to mature solid-state Nd:YAG lasers. Different seawater compositions across coastal and open seas result in varying optimal optical penetration wavelengths. Single-wavelength lidar cannot reveal particle size and absorption effects. Exploring diverse wavelengths in seawater is essential. Using the multi-wavelength volume linear depolarization ratio (VDR) and color ratio measurements from lidar, specific substances in seawater can be identified and distinguished. Meanwhile, in situ measurements are essential for validating the optical properties obtained from marine lidar measurements and for establishing simulation tools for future spaceborne marine lidar missions. In 2022, Liu et al. designed a shipborne variable-FOV, dual-wavelength oceanic P-lidar (as shown in Figure 13), named lidar for Ocean Optics Profiler (LOOP), to obtain the VDR, color ratio, and optical parameter profiles of seawater [63]. High-power pulse lasers and photon-counting detectors effectively increased the detectable seawater depth of the lidar in clean open seas. The system ensured the reliability of oceanic P-lidar by controlling the peak pulse intensity of backscattered signals and calibrating the after-pulse effects of the PMT to maintain the linear response of PMTs, providing seawater backscattered signal profiles. The consistency of the results demonstrated its ability to obtain the optical properties of seawater at certain depths, validating its reliability.

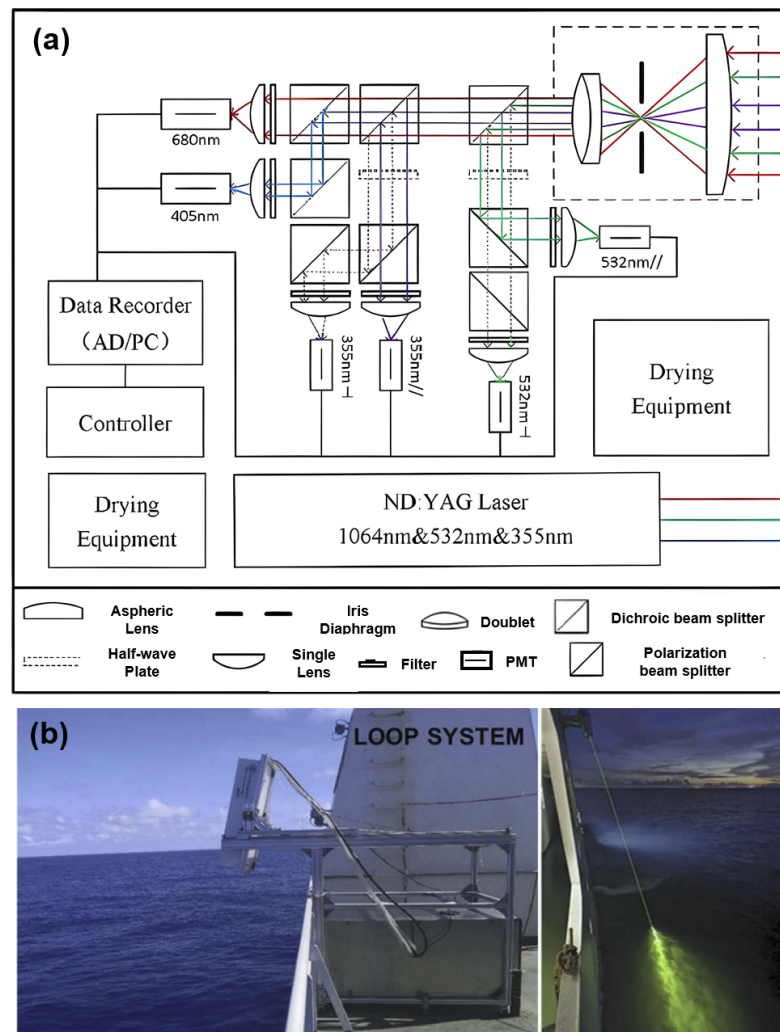


Figure 13. (a) The optical layout and (b) the photo of the LOOP system [63].

Compared to atmospheric or Earth remote sensing, oceanic P-lidar faces greater challenges due to strong seawater attenuation, limiting laser beam penetration. In nearshore seawater, the 532 nm laser energy attenuates by nearly five orders of magnitude when penetrating 30 m deep. Additionally, intense backscattered signals from the sea surface and shallow subsurface seawater can saturate the photodetectors, causing nonlinearity and after-pulse effects, leading to incorrect results. The complex marine environment also complicates accurate VDR. P-lidar for ocean applications, in conjunction with other oceanic measurements, has the potential to revolutionize the capacity for oceanic measurements.

#### 4. Conclusions

This paper systematically reviewed the principles related to P-lidar and introduced the evolution of P-lidar systems from fixed to scanning configurations from an optical perspective. Moreover, we explored the applications of P-lidar technology in various fields, including atmospheric, oceanic, and terrestrial environments, with a special emphasis on intriguing areas such as aerosol detection and classification, ocean profiling, and unmanned driving. Table 1 provides a summary of the P-lidar systems related to various applications discussed in this paper; this also serves as a callback to Figure 3 presented in the Introduction.

**Table 1.** List of representative applications.

Scene	Application	Reference
Atmospheric	Precise all-weather retrieval of atmospheric depolarization ratios	[13]
	Research on the polarization characteristics of various cloud types	[15,132]
	Observe atmospheric ice crystals and water droplets	[39]
	Detect the vertical distribution of aerosols and clouds, ascertain cloud particle phase	[45,143]
	Identify aerosol and cloud types	[53]
	Classification of various aerosol types	[55]
	Measure the depolarization ratio of falling snow	[61,131]
	Detect high-altitude aerosols	[123]
	Retrieve the nonsphericity of ice particles	[125]
	Comprehensive atmospheric measurements	[126]
	Infer the phase state of submicron particles	[127]
	Retrieve micro-physical properties of liquid cloud layers	[128,129]
	Analysis of aerosol and water cloud properties	[130]
	Detect dust orientation	[142]
Study multi-layer aerosol structures	[146]	
Earth surface	Distinguish unique cross-polarization signatures for different tree species	[41]
	Detect smoke from forest fires	[108]
	Infer three-dimensional surface structure of vegetation	[161]
	Characterize the three-dimensional structure of the Earth’s canopy height detection	[162]
	Study vegetation canopy structure and vegetation cross polarization characterization	[165]
	3D imaging in Urban remote sensing	[170]
Autonomous driving	[176]	
Oceanic	Obtain optical properties of seawater at certain depths	[63]
	Detection of scattering layers, fish schools, seawater properties, and internal waves	[67]
	Oceanographic research	[75]
	Observations of aerosols above the ocean	[180]
	Understand the optical and microphysical properties of suspended oceanic particles	[181]
	Measure the polarized light field in the ocean	[182]
	Detection of phytoplankton layers	[184,185]
	Turbulence measurement	[186,187]
	Jellyfish detection	[189,194]
	Retrieval of depolarization optical products in the upper ocean	[190]
Marine biological population detection	[191]	
Sea surface oil spill detection	[196,197]	

Thanks to priors of the polarization differences in target reflection and the polarization characteristics of medium-scattered light, the integration of polarization information acquisition and processing into lidar technology has demonstrated exceptional performance. Recent rapid advancements in both laser source and detector technologies have made it possible to realize multi-channel, multi-spectral (even full-spectral), and full-polarization lidar systems, thereby expanding the application fields of P-lidar. The foundational technologies of P-lidars (e.g., laser sources, polarization detectors, real-time processing algorithms, and system integration) are interdependent and mutually reinforcing.

The increasing demand for practical applications will undoubtedly drive the advancement of P-lidar systems and methodologies. A long-standing pursuit has been the development of a compact and cost-effective P-lidar. The advantage of P-lidar lies in its ability to integrate 3D imaging/detecting and optical material characterization, allowing for the measurement of spectral reflectance and polarimetric reflectance (i.e., represented using Mueller matrices) along with other sensing modalities. Moreover, the demand for miniaturization and cost-effectiveness necessitates novel approaches in designing P-lidar systems, while the need for enhanced target detection and recognition drives research into

light–material interactions and new machine learning algorithms. Based on these insights, we propose several intriguing topics for future research.

*Multi-modal integration:* Integrating P-lidar with various other remote sensing technologies, including traditional lidar, radar, infrared imaging, and more, or merging systems that operate at different wavelengths offers the potential to gather a more-comprehensive set of environmental data. The integration of multiple modalities holds the promise of enhancing our capacity for comprehensive data analysis, enabling a deeper understanding of target recognition and environmental perception. As an illustrative example, Kong et al. designed a visible, near-infrared (Vis–NIR) dual-polarization imaging lidar [55]. Their research demonstrated the system’s remarkable ability to characterize aerosol optical properties, distinguish between different aerosol types, and analyze the long-distance movement of aerosols. This exemplifies the practical advantages of multi-modal integration in environmental sensing. Nevertheless, it is essential to acknowledge that combining multiple sensor modalities also presents certain challenges. These include issues such as data fusion, calibration, synchronization, and increased computational complexity. To fully harness the advantages of integrating diverse sensors, it is imperative to develop appropriate data processing and integration techniques. These solutions will be crucial in overcoming the complexities associated with multi-modal data and ensuring that the combined data streams are effectively utilized.

*Customized P-lidar tailored for oceanic remote sensing:* P-lidar has found mature applications in atmospheric remote sensing. Many airborne or spaceborne P-lidars in use worldwide are primarily tailored for aerosol remote sensing. While it is possible to modify these instruments and systems for ocean color remote sensing, they were not originally designed for this purpose, mainly due to their lower spatial resolution (around 3–4 km). Additionally, ocean polarimetry requires measuring light at an off-principal viewing plane to reduce glint while staying reasonably close to the principal plane to maximize the polarized signal. This preference results in reduced ocean coverage. In ocean applications, it is crucial for the instrument to maintain a very high radiometric accuracy [200,201]. This accuracy is necessary to detect subtle variations in polarized light within the ocean, especially at small scales. Promising solutions include designing advanced sensors with greater sensitivity to polarization measurements and improved noise suppression capabilities. Additionally, the development of spaceborne high-spectral-resolution lidars at wavelengths of 355 and 532 nm is also a viable avenue [202,203].

*Deep-learning-based P-lidar techniques:* Deep learning technology, with its nonlinear convolution operations and powerful implicit correlation learning, leverages the advantages of data-driven approaches to enhance performance in various tasks related to polarization or lidar [204–209]. Compared to traditional intensity-based lidar, P-lidar offers additional information, including time-of-flight data and polarization information. Extracting meaningful features from P-lidar data for use by deep learning models or employing automatic feature selection to enhance model performance is essential. Huang et al. [210] compared distance-resolved aerosol volume concentration (VC) and effective radius (ER) retrieval methods based on partial least-squares regression and deep neural networks (DNNs). They found that the inversion results from DNN outperformed PLSR, particularly in cases with higher VC and ER values. Di Noia et al. (2015) discussed the use of DNN for retrieving the aerosol refractive index, size, and optical depth based on ground-based SPEX measurements [211]. In their subsequent work in 2017, they developed a DNN inversion approach for airborne MAP measurements over land using a research scanning polarimeter [212]. In both studies, the results obtained from DNN inversions were employed as initial values for iterative optimization, resulting in notable improvements in efficiency and retrieval accuracy. However, while using a DNN for direct inversion proves efficient, it is often perceived as a “black box”, making it challenging to account for measurement uncertainties. The combination of DNN inversion with P-lidar’s physical characterizations holds great promise. Besides, in the future, custom-designed deep learning strategies and network

architectures hold the potential to enhance the efficiency of P-lidar in improving resolution, suppressing signal noise, and optimizing radiative transfer iteration.

*Imaging snapshot P-lidar technology:* With the rapid advancement of semiconductor processes and optoelectronic integration techniques, the development of compact, cost-effective, high-resolution, and user-friendly snapshot imaging P-lidar has become possible. In 2021, the California-based startup SiLC Technologies [213] introduced the first commercial chip-level FMCW lidar named “Eyeonic”. Technologically more complex than traditional lidar systems, it has the capability to miniaturize the entire system to chip-level specifications, as shown in Figure 14. In terms of functionality, Eyeonic’s visual sensor showcases an industry-leading detection range of over 1000 m, with three flyovers depicted in different modes, including distance, instantaneous velocity, and polarization intensity, all generating the same point cloud. Another promising direction is to build an imaging P-lidar based on division-of-focal-plane (DoFP) polarization cameras. This involves leveraging the partial polarization characteristics of backscattering light caused by scattering particles in challenging environments such as seawater, low light, or hazy weather [214–217]. This approach can include the development of polarization-suppression algorithms to enhance imaging quality in these complex conditions. Alternatively, constructing a polarimetric-gated lidar imaging device [171,218] can be explored to achieve high-quality imaging in such challenging environments.

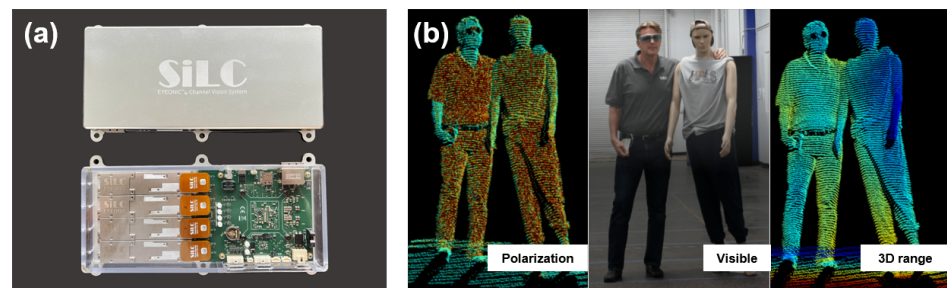


**Figure 14.** (a) The Eyeonic and (b) its output information [213].

*Polarization metasurfaces + lidar:* Even though one of the purposes behind metasurfaces is miniaturization, we still aspire to combine fascinating realms of the metasurfaces technology and P-lidar [219]. Metasurfaces possess the capability to manipulate and control the light state at sub-wavelength scales, presenting a unique opportunity to enhance lidar systems’ performance [220]. For instance, in 2022, a team from South Korea were utilizing metasurfaces to create a solid-state lidar sensor, as illustrated in Figure 15a, which offers a 360° view of the surrounding environment [221]. Almost simultaneously, a team from France proposed an alternative high-frequency beam-scanning approach, harnessing the light-deflecting capabilities of large-area metasurfaces to expand the lidar FOV to  $150 \times 150^\circ$  and achieve simultaneous low- and high-resolution multi-zone imaging, as depicted in Figure 15b [222]. The convergence of polarization metasurfaces and lidar technologies holds immense promise in advancing the field of P-lidars [223,224]. By integrating polarization metasurfaces into lidar sensors, we can anticipate significant improvements in the precision and sensitivity of polarization measurements, enabling the extraction of richer environmental information. This synergy has the potential to revolutionize applications such as remote sensing, autonomous navigation, and atmospheric monitoring, where precise polarization information can unveil new insights and enhance systems’ performance.

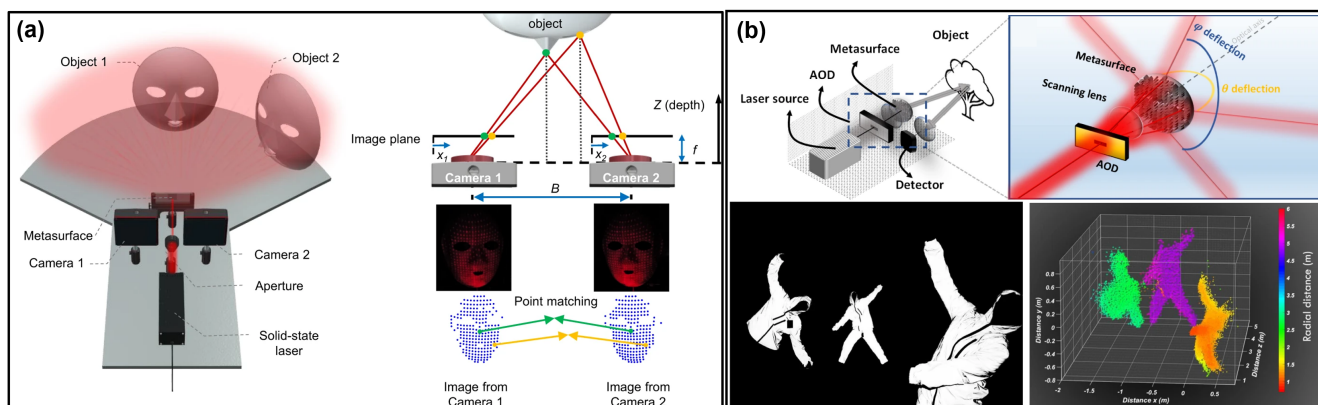


**Figure 15.** (a) Schematic of the optical setup in [221] and the stereo matching algorithm. (b) Schematic representation of the lidar system in [222] and its 3D ranging demonstration.

By addressing these research topics, we can push the boundaries of P-lidar technology, opening up new possibilities for its practical implementation and enhancing its impact in diverse fields.

**Author Contributions:** Conceptualization, X.L. (Xiaobo Li) and X.C.; formal analysis, X.L. (Xudong Liu); investigation, L.Z.; resources, X.L. (Xudong Liu) and L.Z.; data curation, X.L. (Xudong Liu) and X.L. (Xiaobo Li); writing—original draft preparation, X.L. (Xudong Liu), X.L. (Xiaobo Li) and X.C.; writing—review and editing, L.L., X.Z. and Q.Z.; visualization, X.L. (Xudong Liu); supervision, X.L. (Xiaobo Li); project administration, X.L. (Xiaobo Li); funding acquisition, X.L. (Xiaobo Li). All authors have read and agreed to the published version of the manuscript.

**Funding:** This work was supported by the National Natural Science Foundation of China (62205243) and the Key Laboratory of Intelligent Optoelectronics, the Ministry of Education (ZNGD20231001).

**Acknowledgments:** The authors would like to thank all the anonymous reviewers for their helpful comments and suggestions.

**Conflicts of Interest:** The authors declare no conflicts of interest.

## Appendix A

In the paper, all abbreviations used are listed with their full definitions in Table A1.

**Table A1.** List of abbreviations.

Abbreviation	Definition
1C	Single-channel
2C	Dual-channel
4C	Four-channel
3D	Three-dimensional
2D	Two-dimensional
ACEPOL	Aerosol Characterization from Polarimeter and Lidar
ACHSRL	Aerosol and Cloud High-Spectral-Resolution Lidar
ALPS	Airborne Laser Polarization Sensor
APD	Avalanche photodiode
ARM	Atmospheric radiation measurement
CALIOP	Cloud-Aerosol Lidar with Orthogonal Polarization
CAPABL	Clouds Aerosol Polarization and Backscatter Lidar
CCD	Charge-coupled device
CMOS	Complementary metal-oxide semiconductor
DNN	Deep neural network
DoFP	Division-of-focal-plane
DoLP	Degree of linear polarization

Table A1. Cont.

Abbreviation	Definition
DoCP	Degree of circle polarization
EEL	Edge-emitting laser
EMCCD	Electron multiplying charge-coupled devices
FMCW	Frequency-modulated continuous wave
ER	Effective radius
ESA	European Space Agency
EUR	Europe
FOV	Field of view
FR	France
GR	Germany
HERA	Hybrid extinction retrieval algorithm
HSRL	High-spectral-resolution lidar
LASER	Light amplification by stimulated emissions of radiation
LED	Light-emitting diode
Lidar	Light detection and ranging
LOOP	Lidar for Ocean Optics Profiler
LSE	Light's stimulated emission
MEMS	Micro-electro mechanical system
MiniSAR	Miniaturized synthetic aperture radar
MIT	Massachusetts Institute of Technology
MULIS	Multichannel Lidar System
NASA	National Aeronautics and Space Administration
Nd:YAG	Neodymium-doped yttrium aluminum garnet
NOAA	National Oceanic and Atmospheric Administration
OPA	Optical phased array
PBS	Polarization beam splitter
PD	Photodiode
P-Lidar	Polarization lidar
PMT	Photo-multiplier tube
POLIS	Portable lidar system
PSA	Polarization state analyzer
PSG	Polarization state generator
QWP	Quarter-wave plate
RT	Radiative transfer
SCA	Scene classification algorithms
SiPM	Silicon photo-multiplier
SIBYL	Selective Iterative Boundary Locator
SLICER	Scanning Lidar Imager of Canopies by Echo Recovery
SNR	Signal-to-noise ratio
SP	Single-photon
SPAD	Single-photon APD
SVLE	Stokes vector lidar
SWIR	Short-wave infrared
TOF	Time of flight
UAV	Unmanned aerial vehicles
USA	The United States of America
UV	Ultraviolet
VC	Volume concentration
VCSEL	Vertical-cavity surface-emitting laser
Vis-NIR	Visible, near-infrared
VLDR	Volume linear depolarization ratio
WACAL	Water vapor, cloud, and aerosol lidar

## References

1. Pérez, J.J.G.; Ossikovski, R. *Polarized Light and the Mueller Matrix Approach*; CRC Press: Boca Raton, FL, USA, 2017.
2. Goldstein, D.H. *Polarized Light*; CRC Press: Boca Raton, FL, USA, 2017.
3. Bass, M.; Van Stryland, E.W.; Williams, D.R.; Wolfe, W.L. *Handbook of Optics*; McGraw-Hill: New York, NY, USA, 1995; Volume 2.
4. Fowles, G.R. *Introduction to Modern Optics*; Courier Corporation: Washington, DC, USA, 1989.

5. Li, X.; Hu, H.; Zhao, L.; Wang, H.; Yu, Y.; Wu, L.; Liu, T. Polarimetric image recovery method combining histogram stretching for underwater imaging. *Sci. Rep.* **2018**, *8*, 12430. [[CrossRef](#)] [[PubMed](#)]
6. Li, X.; Han, Y.; Wang, H.; Liu, T.; Chen, S.C.; Hu, H. Polarimetric imaging through scattering media: A review. *Front. Phys.* **2022**, *10*, 815296. [[CrossRef](#)]
7. Ballesta-Garcia, M.; Peña-Gutiérrez, S.; Rodríguez-Aramendía, A.; García-Gómez, P.; Rodrigo, N.; Bobi, A.R.; Royo, S. Analysis of the performance of a polarized LiDAR imager in fog. *Opt. Express* **2022**, *30*, 41524–41540. [[CrossRef](#)] [[PubMed](#)]
8. Li, X.; Yan, L.; Qi, P.; Zhang, L.; Goudail, F.; Liu, T.; Zhai, J.; Hu, H. Polarimetric Imaging via Deep Learning: A Review. *Remote Sens.* **2023**, *15*, 1540. [[CrossRef](#)]
9. Chu, J.; Zhao, K.; Zhang, Q.; Wang, T. Construction and performance test of a novel polarization sensor for navigation. *Sens. Actuators Phys.* **2008**, *148*, 75–82. [[CrossRef](#)]
10. Wan, Z.; Zhao, K.; Chu, J. Robust azimuth measurement method based on polarimetric imaging for bionic polarization navigation. *IEEE Trans. Instrum. Meas.* **2019**, *69*, 5684–5692. [[CrossRef](#)]
11. Sun, Z.; Zhang, J.; Zhao, Y. Laboratory studies of polarized light reflection from sea ice and lake ice in visible and near infrared. *IEEE Geosci. Remote. Sens. Lett.* **2012**, *10*, 170–173. [[CrossRef](#)]
12. Sun, W.; Liu, Z.; Videen, G.; Fu, Q.; Muinonen, K.; Winker, D.M.; Lukashin, C.; Jin, Z.; Lin, B.; Huang, J. For the depolarization of linearly polarized light by smoke particles. *J. Quant. Spectrosc. Radiat. Transf.* **2013**, *122*, 233–237. [[CrossRef](#)]
13. Kong, Z.; Ma, T.; Zheng, K.; Cheng, Y.; Gong, Z.; Hua, D.; Mei, L. Development of an all-day portable polarization Lidar system based on the division-of-focal-plane scheme for atmospheric polarization measurements. *Opt. Express* **2021**, *29*, 38512–38526. [[CrossRef](#)]
14. Shibata, Y. Particle polarization Lidar for precipitation particle classification. *Appl. Opt.* **2022**, *61*, 1856–1862. [[CrossRef](#)]
15. Sassen, K. The polarization Lidar technique for cloud research: A review and current assessment. *Bull. Am. Meteorol. Soc.* **1991**, *72*, 1848–1866. [[CrossRef](#)]
16. Sassen, K. Polarization in Lidar. In *LIDAR: Range-Resolved Optical Remote Sensing of the Atmosphere*; Springer: Berlin/Heidelberg, Germany, 2005; pp. 19–42.
17. Einstein, A. Näherungsweise integration der feldgleichungen der gravitation. *Sitzungsberichte Königlich Preussischen Akad. Wiss.* **1916**, *22*, 688–696.
18. Herd, R.M.; Dover, J.S.; Arndt, K.A. Basic laser principles. *Dermatol. Clin.* **1997**, *15*, 355–372. [[CrossRef](#)]
19. Zinth, W.; Laubereau, A.; Kaiser, W. The long journey to the laser and its rapid development after 1960. *Eur. Phys. J. H* **2011**, *36*, 153–181. [[CrossRef](#)]
20. Collis, R. Lidar. *Applied Optics* **1970**, *9*, 1782–1788. [[CrossRef](#)]
21. Dickey, J.O.; Bender, P.; Faller, J.; Newhall, X.; Ricklefs, R.; Ries, J.; Shelus, P.; Veillet, C.; Whipple, A.; Wiant, J.; et al. Lunar laser ranging: A continuing legacy of the Apollo program. *Science* **1994**, *265*, 482–490. [[CrossRef](#)]
22. Bender, P.; Currie, D.; Poultney, S.; Alley, C.; Dicke, R.; Wilkinson, D.; Eckhardt, D.; Faller, J.; Kaula, W.; Mulholland, J.; et al. The Lunar Laser Ranging Experiment: Accurate ranges have given a large improvement in the lunar orbit and new selenophysical information. *Science* **1973**, *182*, 229–238. [[CrossRef](#)]
23. Wandinger, U. Introduction to Lidar. In *Lidar: Range-Resolved Optical Remote Sensing of the Atmosphere*; Springer: Berlin/Heidelberg, Germany, 2005; pp. 1–18.
24. Dubayah, R.O.; Drake, J.B. Lidar remote sensing for forestry. *J. For.* **2000**, *98*, 44–46.
25. Dong, P.; Chen, Q. *LiDAR Remote Sensing and Applications*; CRC Press: Boca Raton, FL, USA, 2017.
26. Han, Y.; Li, Z.; Wu, L.; Mai, S.; Xing, X.; Fu, H. High-Speed Two-Dimensional Spectral-Scanning Coherent LiDAR System Based on Tunable VCSEL. *J. Light. Technol.* **2022**, *41*, 412–419. [[CrossRef](#)]
27. Sun, X.; Zhang, L.; Zhang, Q.; Zhang, W. Si photonics for practical LiDAR solutions. *Appl. Sci.* **2019**, *9*, 4225. [[CrossRef](#)]
28. Shiina, T. LED mini Lidar for atmospheric application. *Sensors* **2019**, *19*, 569. [[CrossRef](#)] [[PubMed](#)]
29. Sarbolandi, H.; Plack, M.; Kolb, A. Pulse based time-of-flight range sensing. *Sensors* **2018**, *18*, 1679. [[CrossRef](#)] [[PubMed](#)]
30. Stove, A.G. Linear FMCW radar techniques. In *IEE Proceedings F (Radar and Signal Processing)*; IET: Washington, DC, USA, 1992; Volume 139, pp. 343–350.
31. McManamon, P.F.; Banks, P.; Beck, J.; Fried, D.G.; Huntington, A.S.; Watson, E.A. Comparison of flash Lidar detector options. *Opt. Eng.* **2017**, *56*, 031223. [[CrossRef](#)]
32. Raj, T.; Hanim Hashim, F.; Baseri Huddin, A.; Ibrahim, M.F.; Hussain, A. A survey on LiDAR scanning mechanisms. *Electronics* **2020**, *9*, 741. [[CrossRef](#)]
33. Tossoun, B.; Stephens, R.; Wang, Y.; Addamane, S.; Balakrishnan, G.; Holmes, A.; Beling, A. High-speed InP-based pin photodiodes with InGaAs/GaAsSb type-II quantum wells. *IEEE Photonics Technol. Lett.* **2018**, *30*, 399–402. [[CrossRef](#)]
34. Villa, F.; Severini, F.; Madonini, F.; Zappa, F. SPADs and SiPMs arrays for long-range high-speed light detection and ranging (LiDAR). *Sensors* **2021**, *21*, 3839. [[CrossRef](#)]
35. Beer, M.; Haase, J.F.; Ruskowski, J.; Kokozinski, R. Background light rejection in SPAD-based LiDAR sensors by adaptive photon coincidence detection. *Sensors* **2018**, *18*, 4338. [[CrossRef](#)] [[PubMed](#)]
36. Behringer, M.; Johnson, K. Laser lightsources for LIDAR. In Proceedings of the 2021 27th International Semiconductor Laser Conference (ISLC), Potsdam, Germany, 10–14 October 2021; pp. 1–2.
37. Wang, D.; Watkins, C.; Xie, H. MEMS mirrors for LiDAR: A review. *Micromachines* **2020**, *11*, 456. [[CrossRef](#)]

38. Li, N.; Ho, C.P.; Xue, J.; Lim, L.W.; Chen, G.; Fu, Y.H.; Lee, L.Y.T. A progress review on solid-state LiDAR and nanophotonics-based LiDAR sensors. *Laser Photonics Rev.* **2022**, *16*, 2100511. [[CrossRef](#)]
39. Schotland, R.M.; Sassen, K.; Stone, R. Observations by Lidar of linear depolarization ratios for hydrometeors. *J. Appl. Meteorol. Climatol.* **1971**, *10*, 1011–1017. [[CrossRef](#)]
40. Platt, C.; Abshire, N.; McNice, G. Some microphysical properties of an ice cloud from Lidar observation of horizontally oriented crystals. *J. Appl. Meteorol. Climatol.* **1978**, *17*, 1220–1224. [[CrossRef](#)]
41. Kalshoven, J.E.; Dabney, P.W. Remote sensing of the Earth's surface with an airborne polarized laser. *IEEE Trans. Geosci. Remote Sens.* **1993**, *31*, 438–446. [[CrossRef](#)]
42. Churnside, J.H. Can we see fish from an airplane? In *Airborne and In-Water Underwater Imaging*; SPIE: Bellingham, WA, USA, 1999; Volume 3761, pp. 45–48.
43. Kaul, B.V.; Samokhvalov, I.V.; Volkov, S.N. Investigating particle orientation in cirrus clouds by measuring backscattering phase matrices with Lidar. *Appl. Opt.* **2004**, *43*, 6620–6628. [[CrossRef](#)] [[PubMed](#)]
44. Del Guasta, M.; Vallar, E.; Riviere, O.; Castagnoli, F.; Venturi, V.; Morandi, M. Use of polarimetric Lidar for the study of oriented ice plates in clouds. *Appl. Opt.* **2006**, *45*, 4878–4887. [[CrossRef](#)] [[PubMed](#)]
45. Winker, D.; Hostetler, C.; Hunt, W. Calipso: The Calipso Lidar. In Proceedings of the 22nd International Laser Radar Conference (ILRC 2004), Matera, Italy, 12–16 July 2004; Volume 561, p. 941.
46. Churnside, J.H.; Sharov, A.F.; Richter, R.A. Aerial surveys of fish in estuaries: A case study in Chesapeake Bay. *ICES J. Mar. Sci.* **2011**, *68*, 239–244. [[CrossRef](#)]
47. Hayman, M.; Thayer, J.P. General description of polarization in Lidar using Stokes vectors and polar decomposition of Mueller matrices. *JOSA A* **2012**, *29*, 400–409. [[CrossRef](#)]
48. Hayman, M.; Spuler, S.; Morley, B.; VanAndel, J. Polarization Lidar operation for measuring backscatter phase matrices of oriented scatterers. *Opt. Express* **2012**, *20*, 29553–29567. [[CrossRef](#)] [[PubMed](#)]
49. Huang, Z.; Qi, S.; Zhou, T.; Dong, Q.; Ma, X.; Zhang, S.; Bi, J.; Shi, J. Investigation of aerosol absorption with dual-polarization Lidar observations. *Opt. Express* **2020**, *28*, 7028–7035. [[CrossRef](#)]
50. Qiu, J.; Xia, H.; Shangguan, M.; Dou, X.; Li, M.; Wang, C.; Shang, X.; Lin, S.; Liu, J. Micro-pulse polarization Lidar at 1.5  $\mu\text{m}$  using a single superconducting nanowire single-photon detector. *Opt. Lett.* **2017**, *42*, 4454–4457. [[CrossRef](#)]
51. Stillwell, R.A.; Neely, R.R., III; Thayer, J.P.; Shupe, M.D.; Turner, D.D. Improved cloud-phase determination of low-level liquid and mixed-phase clouds by enhanced polarimetric Lidar. *Atmos. Meas. Tech.* **2018**, *11*, 835–859. [[CrossRef](#)]
52. Kokhanenko, G.P.; Balin, Y.S.; Klemasheva, M.G.; Nasonov, S.V.; Novoselov, M.M.; Penner, I.E.; Samoilova, S.V. Scanning polarization Lidar LOSA-M3: Opportunity for research of crystalline particle orientation in the ice clouds. *Atmos. Meas. Tech.* **2020**, *13*, 1113–1127. [[CrossRef](#)]
53. Qi, S.; Huang, Z.; Ma, X.; Huang, J.; Zhou, T.; Zhang, S.; Dong, Q.; Bi, J.; Shi, J. Classification of atmospheric aerosols and clouds by use of dual-polarization Lidar measurements. *Opt. Express* **2021**, *29*, 23461–23476. [[CrossRef](#)]
54. Kong, Z.; Ma, T.; Cheng, Y.; Fei, R.; Zhang, Z.; Li, Y.; Mei, L. A polarization-sensitive imaging Lidar for atmospheric remote sensing. *J. Quant. Spectrosc. Radiat. Transf.* **2021**, *271*, 107747. [[CrossRef](#)]
55. Kong, Z.; Yu, J.; Gong, Z.; Hua, D.; Mei, L. Visible, near-infrared dual-polarization Lidar based on polarization cameras: System design, evaluation and atmospheric measurements. *Opt. Express* **2022**, *30*, 28514–28533. [[CrossRef](#)]
56. Hulst, H.C.; van de Hulst, H.C. *Light Scattering by Small Particles*; Courier Corporation: Washington, DC, USA, 1981.
57. Chen, W.; Zheng, Q.; Xiang, H.; Chen, X.; Sakai, T. Forest canopy height estimation using polarimetric interferometric synthetic aperture radar (PolInSAR) technology based on full-polarized ALOS/PALSAR data. *Remote Sens.* **2021**, *13*, 174. [[CrossRef](#)]
58. Buurman, P.; Pape, T.; Muggler, C. Laser grain-size determination in soil genetic studies 1. Practical problems. *Soil Sci.* **1997**, *162*, 211–218. [[CrossRef](#)]
59. Sassen, K.; Zhu, J.; Webley, P.; Dean, K.; Cobb, P. Volcanic ash plume identification using polarization Lidar: Augustine eruption, Alaska. *Geophys. Res. Lett.* **2007**, *34*. [[CrossRef](#)]
60. David, G.; Thomas, B.; Nousiainen, T.; Miffre, A.; Rairoux, P. Retrieving simulated volcanic, desert dust and sea-salt particle properties from two/three-component particle mixtures using UV-VIS polarization Lidar and T matrix. *Atmos. Chem. Phys.* **2013**, *13*, 6757–6776. [[CrossRef](#)]
61. Pal, S.; Carswell, A. The polarization characteristics of Lidar scattering from snow and ice crystals in the atmosphere. *J. Appl. Meteorol. Climatol.* **1977**, *16*, 70–80. [[CrossRef](#)]
62. Gibbs, D.P.; Betty, C.L.; Bredow, J.W.; Fung, A.K. Polarized and cross-polarized angular reflectance characteristics of saline ice and snow. *Remote Sens. Rev.* **1993**, *7*, 179–195. [[CrossRef](#)]
63. Liu, Q.; Wu, S.; Liu, B.; Liu, J.; Zhang, K.; Dai, G.; Tang, J.; Chen, G. Shipborne variable-FOV, dual-wavelength, polarized ocean Lidar: Design and measurements in the Western Pacific. *Opt. Express* **2022**, *30*, 8927–8948. [[CrossRef](#)] [[PubMed](#)]
64. Behrenfeld, M.J.; Hu, Y.; O'Malley, R.T.; Boss, E.S.; Hostetler, C.A.; Siegel, D.A.; Sarmiento, J.L.; Schullien, J.; Hair, J.W.; Lu, X.; et al. Annual boom–bust cycles of polar phytoplankton biomass revealed by space-based Lidar. *Nat. Geosci.* **2017**, *10*, 118–122. [[CrossRef](#)]
65. Behrenfeld, M.J.; Gaube, P.; Della Penna, A.; O'malley, R.T.; Burt, W.J.; Hu, Y.; Bontempi, P.S.; Steinberg, D.K.; Boss, E.S.; Siegel, D.A.; et al. Global satellite-observed daily vertical migrations of ocean animals. *Nature* **2019**, *576*, 257–261. [[CrossRef](#)] [[PubMed](#)]

66. Hoge, F.E.; Wright, C.W.; Krabill, W.B.; Buntzen, R.R.; Gilbert, G.D.; Swift, R.N.; Yungel, J.K.; Berry, R.E. Airborne Lidar detection of subsurface oceanic scattering layers. *Appl. Opt.* **1988**, *27*, 3969–3977. [[CrossRef](#)] [[PubMed](#)]
67. Churnside, J.H. Polarization effects on oceanographic Lidar. *Opt. Express* **2008**, *16*, 1196–1207. [[CrossRef](#)] [[PubMed](#)]
68. Churnside, J.H.; Sullivan, J.M.; Twardowski, M.S. Lidar extinction-to-backscatter ratio of the ocean. *Opt. Express* **2014**, *22*, 18698–18706. [[CrossRef](#)] [[PubMed](#)]
69. Churnside, J.H.; Marchbanks, R.D. Inversion of oceanographic profiling Lidars by a perturbation to a linear regression. *Appl. Opt.* **2017**, *56*, 5228–5233. [[CrossRef](#)]
70. Chen, P.; Jamet, C.; Zhang, Z.; He, Y.; Mao, Z.; Pan, D.; Wang, T.; Liu, D.; Yuan, D. Vertical distribution of subsurface phytoplankton layer in South China Sea using airborne Lidar. *Remote Sens. Environ.* **2021**, *263*, 112567. [[CrossRef](#)]
71. Dassot, M.; Constant, T.; Fournier, M. The use of terrestrial LiDAR technology in forest science: Application fields, benefits and challenges. *Ann. For. Sci.* **2011**, *68*, 959–974. [[CrossRef](#)]
72. Kemeny, J.; Turner, K. *Ground-Based Lidar: Rock Slope Mapping and Assessment*; Technical report; Federal Highway Administration, Central Federal Lands Highway Division: Washington, DC, USA, 2008.
73. Williams, K.; Olsen, M.J.; Roe, G.V.; Glennie, C. Synthesis of transportation applications of mobile LiDAR. *Remote Sens.* **2013**, *5*, 4652–4692. [[CrossRef](#)]
74. Ecke, S.; Dempewolf, J.; Frey, J.; Schwaller, A.; Endres, E.; Klemmt, H.J.; Tiede, D.; Seifert, T. UAV-based forest health monitoring: A systematic review. *Remote Sens.* **2022**, *14*, 3205. [[CrossRef](#)]
75. Vasilkov, A.P.; Goldin, Y.A.; Gureev, B.A.; Hoge, F.E.; Swift, R.N.; Wright, C.W. Airborne polarized Lidar detection of scattering layers in the ocean. *Appl. Opt.* **2001**, *40*, 4353–4364. [[CrossRef](#)] [[PubMed](#)]
76. Goldin, Y.A.; Gureev, B.A.; Ventskut, Y.I. Shipboard polarized Lidar for seawater column sounding. In *Current Research on Remote Sensing, Laser Probing, and Imagery in Natural Waters*; SPIE: Bellingham, WA, USA, 2007; Volume 6615, pp. 152–159.
77. Okamoto, H.; Sato, K.; Borovoi, A.; Ishimoto, H.; Masuda, K.; Konoshonkin, A.; Kustova, N. Interpretation of Lidar ratio and depolarization ratio of ice clouds using spaceborne high-spectral-resolution polarization Lidar. *Opt. Express* **2019**, *27*, 36587–36600. [[CrossRef](#)] [[PubMed](#)]
78. Li, X.; Liu, T.; Huang, B.; Song, Z.; Hu, H. Optimal distribution of integration time for intensity measurements in Stokes polarimetry. *Opt. Express* **2015**, *23*, 27690–27699. [[CrossRef](#)] [[PubMed](#)]
79. Li, X.; Hu, H.; Wu, L.; Liu, T. Optimization of instrument matrix for Mueller matrix ellipsometry based on partial elements analysis of the Mueller matrix. *Opt. Express* **2017**, *25*, 18872–18884. [[CrossRef](#)] [[PubMed](#)]
80. Stokes, G.G. On the composition and resolution of streams of polarized light from different sources. *Trans. Camb. Philos. Soc.* **1851**, *9*, 399.
81. Li, X.; Hu, H.; Liu, T.; Huang, B.; Song, Z. Optimal distribution of integration time for intensity measurements in degree of linear polarization polarimetry. *Opt. Express* **2016**, *24*, 7191–7200. [[CrossRef](#)] [[PubMed](#)]
82. Song, Z.; Li, X.; Liu, T. Optimal distribution of integration time in degree of linear polarization polarimetry based on the expected variance. *Optik* **2017**, *136*, 123–128. [[CrossRef](#)]
83. Chen, W.N.; Chiang, C.W.; Nee, J.B. Lidar ratio and depolarization ratio for cirrus clouds. *Appl. Opt.* **2002**, *41*, 6470–6476. [[CrossRef](#)]
84. Noel, V.; Chepfer, H.; Ledanois, G.; Delaval, A.; Flamant, P.H. Classification of particle effective shape ratios in cirrus clouds based on the Lidar depolarization ratio. *Appl. Opt.* **2002**, *41*, 4245–4257. [[CrossRef](#)]
85. Lu, S.Y.; Chipman, R.A. Interpretation of Mueller matrices based on polar decomposition. *JOSA A* **1996**, *13*, 1106–1113. [[CrossRef](#)]
86. Morio, J.; Goudail, F. Influence of the order of diattenuator, retarder, and polarizer in polar decomposition of Mueller matrices. *Opt. Lett.* **2004**, *29*, 2234–2236. [[CrossRef](#)] [[PubMed](#)]
87. Gil, J.J.; San José, I.; Ossikovski, R. Serial–parallel decompositions of Mueller matrices. *JOSA A* **2013**, *30*, 32–50. [[CrossRef](#)] [[PubMed](#)]
88. Li, X.; Zhang, L.; Qi, P.; Zhu, Z.; Xu, J.; Liu, T.; Zhai, J.; Hu, H. Are indices of polarimetric purity excellent metrics for object identification in scattering media? *Remote Sens.* **2022**, *14*, 4148. [[CrossRef](#)]
89. Li, X.; Liu, W.; Goudail, F.; Chen, S.C. Optimal nonlinear Stokes—Mueller polarimetry for multi-photon processes. *Opt. Lett.* **2022**, *47*, 3287–3290. [[CrossRef](#)] [[PubMed](#)]
90. Li, X.; Goudail, F.; Chen, S.C. Self-calibration for Mueller polarimeters based on DoFP polarization imagers. *Opt. Lett.* **2022**, *47*, 1415–1418. [[CrossRef](#)] [[PubMed](#)]
91. Chandrasekar, V.; Keränen, R.; Lim, S.; Moisseev, D. Recent advances in classification of observations from dual polarization weather radars. *Atmos. Res.* **2013**, *119*, 97–111. [[CrossRef](#)]
92. Sassen, K.; Wang, Z.; Liu, D. Global distribution of cirrus clouds from CloudSat/Cloud-Aerosol Lidar and infrared pathfinder satellite observations (CALIPSO) measurements. *J. Geophys. Res. Atmos.* **2008**, *113*, D8. [[CrossRef](#)]
93. Ahmad, W.; Zhang, K.; Tong, Y.; Xiao, D.; Wu, L.; Liu, D. Water cloud detection with circular polarization Lidar: A semianalytic Monte Carlo simulation approach. *Sensors* **2022**, *22*, 1679. [[CrossRef](#)]
94. Evans, B.T.N. *On the Inversion of the Lidar Equation*; Department of National Defence, Research and Development Branch, Defence Research Establishment: Umea, Sweden, 1984.
95. Northend, C.; Honey, R.; Evans, W. Laser radar (Lidar) for meteorological observations. *Rev. Sci. Instrum.* **1966**, *37*, 393–400. [[CrossRef](#)]

96. Sasano, Y.; Shimizu, H.; Takeuchi, N.; Okuda, M. Geometrical form factor in the laser radar equation: An experimental determination. *Appl. Opt.* **1979**, *18*, 3908–3910. [CrossRef] [PubMed]
97. Biele, J.; Beyerle, G.; Baumgarten, G. Polarization Lidar: Corrections of instrumental effects. *Opt. Express* **2000**, *7*, 427–435. [CrossRef] [PubMed]
98. Freudenthaler, V. About the effects of polarising optics on Lidar signals and the  $\Delta 90$  calibration. *Atmos. Meas. Tech.* **2016**, *9*, 4181–4255. [CrossRef]
99. Winker, D.M.; Vaughan, M.A.; Omar, A.; Hu, Y.; Powell, K.A.; Liu, Z.; Hunt, W.H.; Young, S.A. Overview of the CALIPSO mission and CALIOP data processing algorithms. *J. Atmos. Ocean. Technol.* **2009**, *26*, 2310–2323. [CrossRef]
100. Winker, D.M.; Hunt, W.H.; McGill, M.J. Initial performance assessment of CALIOP. *Geophys. Res. Lett.* **2007**, *34*, 19. [CrossRef]
101. Winker, D.; Pelon, J.; Coakley, J., Jr.; Ackerman, S.; Charlson, R.; Colarco, P.; Flamant, P.; Fu, Q.; Hoff, R.; Kittaka, C.; et al. The CALIPSO mission: A global 3D view of aerosols and clouds. *Bull. Am. Meteorol. Soc.* **2010**, *91*, 1211–1230. [CrossRef]
102. Sarabandi, K.; Ulaby, F.T.; Tassoudji, M.A. Calibration of polarimetric radar systems with good polarization isolation. *IEEE Trans. Geosci. Remote Sens.* **1990**, *28*, 70–75. [CrossRef]
103. Alvarez, J.; Vaughan, M.A.; Hostetler, C.A.; Hunt, W.; Winker, D.M. Calibration technique for polarization-sensitive Lidars. *J. Atmos. Ocean. Technol.* **2006**, *23*, 683–699. [CrossRef]
104. Platt, C. Lidar observation of a mixed-phase altostratus cloud. *J. Appl. Meteorol. Climatol.* **1977**, *16*, 339–345. [CrossRef]
105. Flynn, C.J.; Mendoza, A.; Zheng, Y.; Mathurb, S. Novel polarization-sensitive micropulse Lidar measurement technique. *Opt. Express* **2007**, *15*, 2785–2790. [CrossRef]
106. Pal, S.; Carswell, A. Polarization properties of Lidar backscattering from clouds. *Appl. Opt.* **1973**, *12*, 1530–1535. [CrossRef] [PubMed]
107. Houston, J.; Carswell, A. Four-component polarization measurement of Lidar atmospheric scattering. *Appl. Opt.* **1978**, *17*, 614–620. [CrossRef] [PubMed]
108. Xian, J.; Xu, W.; Long, C.; Song, Q.; Yang, S. Early forest-fire detection using scanning polarization Lidar. *Appl. Opt.* **2020**, *59*, 8638–8644. [CrossRef] [PubMed]
109. Noel, V.; Sassen, K. Study of planar ice crystal orientations in ice clouds from scanning polarization Lidar observations. *J. Appl. Meteorol. Climatol.* **2005**, *44*, 653–664. [CrossRef]
110. Sassen, K. Polarization in Lidar: A review. *Polariz. Sci. Remote Sens.* **2003**, *5158*, 151–160.
111. Li, C.; Xu, S.; Zhao, L.; Cheng, G. Research on MEMS biaxial electromagnetic micromirror based on radial magnetic field distribution. In Proceedings of the International Conference on Laser, Optics and Optoelectronic Technology (LOPET 2021), Xi'an, China, 28–30 May 2021; Volume 11885, pp. 206–212.
112. Roriz, R.; Cabral, J.; Gomes, T. Automotive LiDAR technology: A survey. *IEEE Trans. Intell. Transp. Syst.* **2021**, *23*, 6282–6297. [CrossRef]
113. Kokhanenko, G.P. Possibilities of using mirror scanners in polarizing Lidars. In Proceedings of the 28th International Symposium on Atmospheric and Ocean Optics: Atmospheric Physics, Tomsk, Russia, 4–8 July 2022; Volume 12341, pp. 328–333.
114. Li, X.; Li, Y.; Xie, X.; Xu, L. Laser polarization imaging models based on leaf moisture content (in Chinese). *Infrared Laser Eng.* **2017**, *46*, 1106004.
115. Behrendt, A.; Nakamura, T. Calculation of the calibration constant of polarization Lidar and its dependency on atmospheric temperature. *Opt. Express* **2002**, *10*, 805–817. [CrossRef]
116. Luo, J.; Liu, D.; Bi, L.; Zhang, K.; Tang, P.; Xu, P.; Su, L.; Yang, L. Rotating a half-wave plate by 45: An ideal calibration method for the gain ratio in polarization Lidars. *Opt. Commun.* **2018**, *407*, 361–366. [CrossRef]
117. Mattis, I.; Tesche, M.; Grein, M.; Freudenthaler, V.; Müller, D. Systematic error of Lidar profiles caused by a polarization-dependent receiver transmission: Quantification and error correction scheme. *Appl. Opt.* **2009**, *48*, 2742–2751. [CrossRef]
118. Hunt, W.H.; Winker, D.M.; Vaughan, M.A.; Powell, K.A.; Lucker, P.L.; Weimer, C. CALIPSO Lidar description and performance assessment. *J. Atmos. Ocean. Technol.* **2009**, *26*, 1214–1228. [CrossRef]
119. Sassen, K.; Benson, S. A midlatitude cirrus cloud climatology from the Facility for Atmospheric Remote Sensing. Part II: Microphysical properties derived from Lidar depolarization. *J. Atmos. Sci.* **2001**, *58*, 2103–2112. [CrossRef]
120. Tong, Y.; Tong, X.; Zhang, K.; Xiao, D.; Rong, Y.; Zhou, Y.; Liu, C.; Liu, D. Polarization Lidar gain ratio calibration method: A comparison. *Chin. Opt.* **2021**, *14*, 685–703.
121. Luo, J.; Liu, D.; Huang, Z.; Wang, B.; Bai, J.; Cheng, Z.; Zhang, Y.; Tang, P.; Yang, L.; Su, L. Polarization properties of receiving telescopes in atmospheric remote sensing polarization Lidars. *Appl. Opt.* **2017**, *56*, 6837–6845. [CrossRef] [PubMed]
122. Freudenthaler, V.; Esselborn, M.; Wiegner, M.; Heese, B.; Tesche, M.; Ansmann, A.; Müller, D.; Althausen, D.; Wirth, M.; Fix, A.; et al. Depolarization ratio profiling at several wavelengths in pure Saharan dust during SAMUM 2006. *Tellus Chem. Phys. Meteorol.* **2009**, *61*, 165–179. [CrossRef]
123. Fiocco, G.; Smullin, L. Detection of scattering layers in the upper atmosphere (60–140 km) by optical radar. *Nature* **1963**, *199*, 1275–1276. [CrossRef]
124. Polarization Lidar. Available online: <https://www.tropos.de/en/research/projects-infrastructure-technology/technology-at-tropos/remote-sensing/polarization-Lidar> (accessed on 3 September 2023).
125. Matrosov, S.Y.; Schmitt, C.G.; Maahn, M.; de Boer, G. Atmospheric ice particle shape estimates from polarimetric radar measurements and in situ observations. *J. Atmos. Ocean. Technol.* **2017**, *34*, 2569–2587. [CrossRef]

126. Wu, S.; Song, X.; Liu, B.; Dai, G.; Liu, J.; Zhang, K.; Qin, S.; Hua, D.; Gao, F.; Liu, L. Mobile multi-wavelength polarization Raman Lidar for water vapor, cloud and aerosol measurement. *Opt. Express* **2015**, *23*, 33870–33892. [[CrossRef](#)]
127. Tan, W.; Li, C.; Liu, Y.; Meng, X.; Wu, Z.; Kang, L.; Zhu, T. Potential of polarization Lidar to profile the urban aerosol phase state during haze episodes. *Environ. Sci. Technol. Lett.* **2019**, *7*, 54–59. [[CrossRef](#)]
128. Jimenez, C.; Ansmann, A.; Engelmann, R.; Donovan, D.; Malinka, A.; Jörg, S.; Patric, S.; Ulla, W. The dual-field-of-view polarization Lidar technique: A new concept in monitoring aerosol effects in liquid-water clouds—Theoretical framework. *Atmos. Chem. Phys.* **2020**, *20*, 15247–15263. [[CrossRef](#)]
129. Jimenez, C.; Ansmann, A.; Engelmann, R.; Donovan, D.; Malinka, A.; Seifert, P.; Wiesen, R.; Radenz, M.; Yin, Z.; Bühl, J.; et al. The dual-field-of-view polarization Lidar technique: A new concept in monitoring aerosol effects in liquid-water clouds—Case studies. *Atmos. Chem. Phys.* **2020**, *20*, 15265–15284. [[CrossRef](#)]
130. Zhang, S.; Huang, Z.; Alam, K.; Li, M.; Dong, Q.; Wang, Y.; Shen, X.; Bi, J.; Zhang, J.; Li, W.; et al. Derived Profiles of CCN and INP Number Concentrations in the Taklimakan Desert via Combined Polarization Lidar, Sun-Photometer, and Radiosonde Observations. *Remote Sens.* **2023**, *15*, 1216. [[CrossRef](#)]
131. Pal, S.; Carswell, A. Polarization properties of Lidar scattering from clouds at 347 nm and 694 nm. *Appl. Opt.* **1978**, *17*, 2321–2328. [[CrossRef](#)] [[PubMed](#)]
132. Sassen, K.; Zhao, H.; Dodd, G.C. Simulated polarization diversity Lidar returns from water and precipitating mixed phase clouds. *Appl. Opt.* **1992**, *31*, 2914–2923. [[CrossRef](#)]
133. Mamouri, R.E.; Ansmann, A. Potential of polarization Lidar to provide profiles of CCN-and INP-relevant aerosol parameters. *Atmos. Chem. Phys.* **2016**, *16*, 5905–5931. [[CrossRef](#)]
134. Ansmann, A.; Ohneiser, K.; Mamouri, R.E.; Knopf, D.A.; Veselovskii, I.; Baars, H.; Engelmann, R.; Foth, A.; Jimenez, C.; Seifert, P.; et al. Tropospheric and stratospheric wildfire smoke profiling with Lidar: Mass, surface area, CCN, and INP retrieval. *Atmos. Chem. Phys.* **2021**, *21*, 9779–9807. [[CrossRef](#)]
135. Murayama, T.; Müller, D.; Wada, K.; Shimizu, A.; Sekiguchi, M.; Tsukamoto, T. Characterization of Asian dust and Siberian smoke with multi-wavelength Raman Lidar over Tokyo, Japan in spring 2003. *Geophys. Res. Lett.* **2004**, *31*, 23. [[CrossRef](#)]
136. Sugimoto, N.; Lee, C.H. Characteristics of dust aerosols inferred from Lidar depolarization measurements at two wavelengths. *Appl. Opt.* **2006**, *45*, 7468–7474. [[CrossRef](#)]
137. Sugimoto, N.; Uno, I.; Nishikawa, M.; Shimizu, A.; Matsui, I.; Dong, X.; Chen, Y.; Quan, H. Record heavy Asian dust in Beijing in 2002: Observations and model analysis of recent events. *Geophys. Res. Lett.* **2003**, *30*, 12. [[CrossRef](#)]
138. Tesche, M.; Ansmann, A.; Müller, D.; Althausen, D.; Engelmann, R.; Freudenthaler, V.; Groß, S. Vertically resolved separation of dust and smoke over Cape Verde using multiwavelength Raman and polarization Lidars during Saharan Mineral Dust Experiment 2008. *J. Geophys. Res. Atmos.* **2009**, *114*, D13. [[CrossRef](#)]
139. Burton, S.; Hair, J.; Kahnert, M.; Ferrare, R.; Hostetler, C.; Cook, A.; Harper, D.; Berkoff, T.; Seaman, S.; Collins, J.; et al. Observations of the spectral dependence of linear particle depolarization ratio of aerosols using NASA Langley airborne High Spectral Resolution Lidar. *Atmos. Chem. Phys.* **2015**, *15*, 13453–13473. [[CrossRef](#)]
140. Haerig, M.; Althausen, D.; Ansmann, A.; Klepel, A.; Baars, H.; Engelmann, R.; Groß, S.; Freudenthaler, V. Measurement of the linear depolarization ratio of aged dust at three wavelengths (355, 532 and 1064 nm) simultaneously over Barbados. In *EPJ Web of Conferences*; EDP Sciences: Les Ulis, France, 2016; Volume 119, p. 18009.
141. Vaughan, M.; Garnier, A.; Josset, D.; Avery, M.; Lee, K.P.; Liu, Z.; Hunt, W.; Pelon, J.; Hu, Y.; Burton, S.; et al. CALIPSO Lidar calibration at 1064 nm: Version 4 algorithm. *Atmos. Meas. Tech.* **2019**, *12*, 51–82. [[CrossRef](#)]
142. Tsekeri, A.; Amiridis, V.; Louridas, A.; Georgoussis, G.; Freudenthaler, V.; Metallinos, S.; Doxastakis, G.; Gasteiger, J.; Siomos, N.; Paschou, P.; et al. Polarization Lidar for detecting dust orientation: System design and calibration. *Atmos. Meas. Tech.* **2021**, *14*, 7453–7474. [[CrossRef](#)]
143. Seckar, C.; Guy, L.; DiFronzo, A.; Weimer, C. Performance testing of an active boresight mechanism for use in the CALIPSO space borne LIDAR mission. In *Optomechanics 2005*; SPIE: Bellingham, WA, USA, 2005; Volume 5877, pp. 319–330.
144. Atmospheric Aerosol Characterization. Available online: <https://www.ll.mit.edu/r-d/projects/atmospheric-aerosol-characterization> (accessed on 3 September 2023).
145. Knobelspiesse, K.; Barbosa, H.M.; Bradley, C.; Bruegge, C.; Cairns, B.; Chen, G.; Chowdhary, J.; Cook, A.; Di Noia, A.; van Diedenhoven, B.; et al. The Aerosol Characterization from Polarimeter and Lidar (ACEPOL) airborne field campaign. *Earth Syst. Sci. Data Discuss.* **2020**, *2020*, 1–38. [[CrossRef](#)]
146. Dulac, F.; Chazette, P. Airborne study of a multi-layer aerosol structure in the eastern Mediterranean observed with the airborne polarized Lidar ALEX during a STAAARTE campaign (7 June 1997). *Atmos. Chem. Phys.* **2003**, *3*, 1817–1831. [[CrossRef](#)]
147. Bo, G.; Liu, D.; Wang, B.; Wu, D.; Zhong, Z. Two-wavelength polarization airborne Lidar for observation of aerosol and cloud. *Zhongguo Jiguang Chin. J. Lasers* **2012**, *39*, 1014002-6.
148. Fernald, F.G.; Herman, B.M.; Reagan, J.A. Determination of aerosol height distributions by Lidar. *J. Appl. Meteorol. Climatol.* **1972**, *11*, 482–489. [[CrossRef](#)]
149. Klett, J.D. Stable analytical inversion solution for processing Lidar returns. *Appl. Opt.* **1981**, *20*, 211–220. [[CrossRef](#)] [[PubMed](#)]
150. Davis, P. The analysis of Lidar signatures of cirrus clouds. *Appl. Opt.* **1969**, *8*, 2099–2102. [[CrossRef](#)]
151. Sasano, Y.; Nakane, H. Significance of the extinction/backscatter ratio and the boundary value term in the solution for the two-component Lidar equation. *Appl. Opt.* **1984**, *23*, 11–13. [[CrossRef](#)]

152. Hinkley, E.D. *Laser Monitoring of the Atmosphere*; Springer: Berlin, Germany, 1976.
153. Fernald, F.G. Analysis of atmospheric Lidar observations: Some comments. *Appl. Opt.* **1984**, *23*, 652–653. [CrossRef] [PubMed]
154. Dawson, K.; Ferrare, R.; Moore, R.; Clayton, M.; Thorsen, T.; Eloranta, E. Ambient aerosol hygroscopic growth from combined Raman Lidar and HSRL. *J. Geophys. Res. Atmos.* **2020**, *125*, e2019JD031708. [CrossRef]
155. Liu, Z.; Sugimoto, N.; Murayama, T. Extinction-to-backscatter ratio of Asian dust observed with high-spectral-resolution Lidar and Raman Lidar. *Appl. Opt.* **2002**, *41*, 2760–2767. [CrossRef] [PubMed]
156. Thorsen, T.J.; Fu, Q. Automated retrieval of cloud and aerosol properties from the ARM Raman Lidar. Part II: Extinction. *J. Atmos. Ocean. Technol.* **2015**, *32*, 1999–2023. [CrossRef]
157. Thorsen, T.J.; Fu, Q.; Newsom, R.K.; Turner, D.D.; Comstock, J.M. Automated retrieval of cloud and aerosol properties from the ARM Raman Lidar. Part I: Feature detection. *J. Atmos. Ocean. Technol.* **2015**, *32*, 1977–1998. [CrossRef]
158. Ferrare, R.A.; Thorsen, T.; Clayton, M.; Muller, D.; Chernyakin, E.; Burton, S.; Goldsmith, J.; Holz, R.; Kuehn, R.; Eloranta, E.; et al. *Vertically Resolved Retrievals of Aerosol Concentrations and Effective Radii from the DOE Combined HSRL and Raman Lidar Measurement Study (CHARMS) Merged High-Spectral-Resolution Lidar-Raman Lidar Data Set*; Technical report; DOE Office of Science Atmospheric Radiation Measurement (ARM) Program: Washington, DC, USA, 2017.
159. Sorrentino, A.; Sannino, A.; Spinelli, N.; Piana, M.; Boselli, A.; Tontodonato, V.; Castellano, P.; Wang, X. A Bayesian parametric approach to the retrieval of the atmospheric number size distribution from Lidar data. *Atmos. Meas. Tech.* **2022**, *15*, 149–164. [CrossRef]
160. Ke, J.; Sun, Y.; Dong, C.; Zhang, X.; Wang, Z.; Lyu, L.; Zhu, W.; Ansmann, A.; Su, L.; Bu, L.; et al. Development of China's first space-borne aerosol-cloud high-spectral-resolution Lidar: Retrieval algorithm and airborne demonstration. *PhotoniX* **2022**, *3*, 17. [CrossRef]
161. Harding, D. *SLICER Airborne Laser Altimeter Characterization of Canopy Structure and Sub-Canopy Topography for the BOREAS Northern and Southern Study Regions: Instrument and Data Product Description*; National Aeronautics and Space Administration, Goddard Space Flight Center: Pasadena, CA, USA, 2000.
162. Dubayah, R.; Prince, S.; JaJa, J.; Blair, J.; Bufton, J.L.; Knox, R.; Luthcke, S.B.; Clarke, D.B.; Weishampel, J. The vegetation canopy Lidar mission. In *Land Satellite Information in the Next Decade II: Sources and Applications*; 1997. Available online: <https://www.umiacs.umd.edu/publications/vegetation-canopy-lidar-mission> (accessed on 3 September 2023).
163. Kalshoven, J.E.; Tierney, M.R.; Daughtry, C.S.; McMurtrey, J.E. Remote sensing of crop parameters with a polarized, frequency-doubled Nd: YAG laser. *Appl. Opt.* **1995**, *34*, 2745–2749. [CrossRef]
164. Tan, S.; Narayanan, R.M. A multiwavelength airborne polarimetric Lidar for vegetation remote sensing: Instrumentation and preliminary test results. *IEEE Int. Geosci. Remote. Sens. Symp.* **2002**, *5*, 2675–2677.
165. Tan, S.; Narayanan, R.M. Design and performance of a multiwavelength airborne polarimetric Lidar for vegetation remote sensing. *Appl. Opt.* **2004**, *43*, 2360–2368. [CrossRef]
166. Tan, S.; Narayanan, R.M.; Helder, D.L. Polarimetric reflectance and depolarization ratio from several tree species using a multiwavelength polarimetric Lidar. In *Polarization Science and Remote Sensing II*; SPIE: Bellingham, WA, USA, 2005; Volume 5888, pp. 180–188.
167. Tan, S.; Johnson, S.; Gu, Z. Laser depolarization ratio measurement of corn leaves from the biochar and non-biochar applied plots. *Opt. Express* **2018**, *26*, 14295–14306. [CrossRef] [PubMed]
168. Andreucci, F.; Arbolino, M. A study on forest fire automatic detection systems: I.—Smoke plume model. *Il Nuovo C. C* **1993**, *16*, 35–50. [CrossRef]
169. Vaughan, G.; Draude, A.P.; Ricketts, H.M.; Schultz, D.M.; Adam, M.; Sugier, J.; Wareing, D.P. Transport of Canadian forest fire smoke over the UK as observed by Lidar. *Atmos. Chem. Phys.* **2018**, *18*, 11375–11388. [CrossRef]
170. Taboada, J.; Tamburino, L.A. Laser Imaging and Ranging System Using Two Cameras. U.S. Patent 5,157,451, 20 October 1992.
171. Chen, Z.; Liu, B.; Liu, E.; Peng, Z. Adaptive polarization-modulated method for high-resolution 3D imaging. *IEEE Photonics Technology Letters* **2015**, *28*, 295–298. [CrossRef]
172. Chen, Z.; Liu, B.; Wang, S.; Liu, E. Polarization-modulated three-dimensional imaging using a large-aperture electro-optic modulator. *Appl. Opt.* **2018**, *57*, 7750–7757. [CrossRef] [PubMed]
173. Li, X.; Hu, H.; Goudail, F.; Liu, T. Fundamental precision limits of full Stokes polarimeters based on DoFP polarization cameras for an arbitrary number of acquisitions. *Opt. Express* **2019**, *27*, 31261–31272. [CrossRef] [PubMed]
174. Li, X.; Le Teurnier, B.; Boffety, M.; Liu, T.; Hu, H.; Goudail, F. Theory of autocalibration feasibility and precision in full Stokes polarization imagers. *Opt. Express* **2020**, *28*, 15268–15283. [CrossRef] [PubMed]
175. Jo, S.; Kong, H.J.; Bang, H.; Kim, J.W.; Kim, J.; Choi, S. High resolution three-dimensional flash LIDAR system using a polarization modulating Pockels cell and a micro-polarizer CCD camera. *Opt. Express* **2016**, *24*, A1580–A1585. [CrossRef]
176. Nunes-Pereira, E.; Peixoto, H.; Teixeira, J.; Santos, J. Polarization-coded material classification in automotive LIDAR aiming at safer autonomous driving implementations. *Appl. Opt.* **2020**, *59*, 2530–2540. [CrossRef]
177. Ronen, A.; Agassi, E.; Yaron, O. Sensing with polarized Lidar in degraded visibility conditions due to fog and low clouds. *Sensors* **2021**, *21*, 2510. [CrossRef]
178. Kattawar, G.W.; Plass, G.N.; Guinn, J.A., Jr. Monte Carlo calculations of the polarization of radiation in the earth's atmosphere-ocean system. *J. Phys. Oceanogr.* **1973**, *3*, 353–372. [CrossRef]

179. Chowdhary, J.; Cairns, B.; Travis, L.D. Contribution of water-leaving radiances to multiangle, multispectral polarimetric observations over the open ocean: Bio-optical model results for case 1 waters. *Appl. Opt.* **2006**, *45*, 5542–5567. [[CrossRef](#)] [[PubMed](#)]
180. Chowdhary, J.; Cairns, B.; Waquet, F.; Knobelspiesse, K.; Ottaviani, M.; Redemann, J.; Travis, L.; Mishchenko, M. Sensitivity of multiangle, multispectral polarimetric remote sensing over open oceans to water-leaving radiance: Analyses of RSP data acquired during the MILAGRO campaign. *Remote Sens. Environ.* **2012**, *118*, 284–308. [[CrossRef](#)]
181. Chami, M. Importance of the polarization in the retrieval of oceanic constituents from the remote sensing reflectance. *J. Geophys. Res. Ocean* **2007**, *112*, C5. [[CrossRef](#)]
182. Tonizzo, A.; Zhou, J.; Gilerson, A.; Twardowski, M.S.; Gray, D.J.; Arnone, R.A.; Gross, B.M.; Moshary, F.; Ahmed, S.A. Polarized light in coastal waters: Hyperspectral and multiangular analysis. *Opt. Express* **2009**, *17*, 5666–5683. [[CrossRef](#)] [[PubMed](#)]
183. Voss, K.J.; Souaidia, N. POLRADs: Polarization radiance distribution measurement system. *Opt. Express* **2010**, *18*, 19672–19680. [[CrossRef](#)] [[PubMed](#)]
184. Churnside, J.H. Review of profiling oceanographic Lidar. *Opt. Eng.* **2014**, *53*, 051405–051405. [[CrossRef](#)]
185. Yang, Y.; Pan, H.; Zheng, D.; Zhao, H.; Zhou, Y.; Liu, D. Characteristics and Formation Conditions of Thin Phytoplankton Layers in the Northern Gulf of Mexico Revealed by Airborne Lidar. *Remote Sens.* **2022**, *14*, 4179. [[CrossRef](#)]
186. Woods, S.; Piskozub, J.; Freda, W.; Jonasz, M.; Bogucki, D. Laboratory measurements of light beam depolarization on turbulent convective flow. *Appl. Opt.* **2010**, *49*, 3545–3551. [[CrossRef](#)]
187. Bogucki, D.J.; Domaradzki, J.A.; von Allmen, P. Polarimetric Lidar measurements of aquatic turbulence-laboratory experiment. *Opt. Express* **2018**, *26*, 6806–6816. [[CrossRef](#)]
188. Churnside, J.H.; Wilson, J.J.; Tatarskii, V.V. Lidar profiles of fish schools. *Appl. Opt.* **1997**, *36*, 6011–6020. [[CrossRef](#)] [[PubMed](#)]
189. Churnside, J.H.; Marchbanks, R.D.; Donaghay, P.L.; Sullivan, J.M.; Graham, W.M.; Wells, R.D. Hollow aggregations of moon jellyfish (*Aurelia* spp.). *J. Plankton Res.* **2016**, *38*, 122–130. [[CrossRef](#)]
190. Collister, B.L.; Zimmerman, R.C.; Sukenik, C.I.; Hill, V.J.; Balch, W.M. Remote sensing of optical characteristics and particle distributions of the upper ocean using shipboard Lidar. *Remote Sens. Environ.* **2018**, *215*, 85–96. [[CrossRef](#)]
191. Murphree, D.L.; Taylor, C.D.; McClendon, R.W. Mathematical modeling for the detection of fish by an airborne laser. *Aiaa J.* **1974**, *12*, 1686–1692. [[CrossRef](#)]
192. Fredriksson, K.; Galle, B.; Nystrom, K. Underwater laser-radar experiments for bathymetry and fish school detection: Report GJPR-162, Göteborg Inst. *Phys. Göteborg.* **1978**, *162*, 1–28.
193. Shamanaev, V. Detection of schools of marine fish using polarization laser sensing. *Atmos. Ocean. Opt.* **2018**, *31*, 358–364. [[CrossRef](#)]
194. Wang, X.; Zhao, K.; Zhou, Y.; Zhang, F.; Xu, P.; Liu, Q.; Liu, C.; Liu, D. Characteristics of jellyfish in the Yellow Sea detected by polarized oceanic Lidar. *Infrared Laser Eng.* **2021**, *50*, 20211038-1. (In Chinese)
195. Fingas, M.; Brown, C.E. A review of oil spill remote sensing. *Sensors* **2017**, *18*, 91. [[CrossRef](#)]
196. Hengstermann, T.; Reuter, R. Lidar fluorosensing of mineral oil spills on the sea surface. *Appl. Opt.* **1990**, *29*, 3218–3227. [[CrossRef](#)]
197. Jha, M.N.; Levy, J.; Gao, Y. Advances in remote sensing for oil spill disaster management: State-of-the-art sensors technology for oil spill surveillance. *Sensors* **2008**, *8*, 236–255. [[CrossRef](#)]
198. Wang, Z.; Zhang, Y.; Liu, D.; Wang, X.; Yuan, J.; Pan, C.; Zhao, Y.; Han, X.; Zhou, Y.; Liu, Q.; et al. Research on the development of detection satellite technology in the novel multi-beam land and ocean Lidar. *Infrared Laser Eng.* **2021**, *50*, 20211041. (In Chinese)
199. Zhao, C.; Li, X.; Ma, Y. Multi-channel ocean fluorescence Lidar system for oil spill monitoring. *Infrared Laser Eng.* **2011**, *40*, 1263–1269. (In Chinese)
200. Jamet, C.; Ibrahim, A.; Ahmad, Z.; Angelini, F.; Babin, M.; Behrenfeld, M.J.; Boss, E.; Cairns, B.; Churnside, J.; Chowdhary, J.; et al. Going beyond standard ocean color observations: Lidar and polarimetry. *Front. Mar. Sci.* **2019**, *6*, 251. [[CrossRef](#)]
201. Zhang, W.; Li, X.; Xu, S.; Li, X.; Yang, Y.; Xu, D.; Liu, T.; Hu, H. Underwater Image Restoration via Adaptive Color Correction and Contrast Enhancement Fusion. *Remote Sens.* **2023**, *15*, 4699. [[CrossRef](#)]
202. Hair, J.; Hostetler, C.; Hu, Y.; Behrenfeld, M.; Butler, C.; Harper, D.; Hare, R.; Berkoff, T.; Cook, A.; Collins, J.; et al. Combined atmospheric and ocean profiling from an airborne high spectral resolution Lidar. In *EPJ Web of Conferences*; EDP Sciences: Les Ulis, France, 2016; Volume 119, p. 22001.
203. Zhao, H.; Shi, H.; Xu, P.; Qian, Z.; Xu, X.; Li, Z.; Zhai, J.; Li, X.; Xue, B. Direct Measurement of Underwater Sound Velocity via Dual-Comb System and Matched Filtering Algorithm. *IEEE Trans. Instrum. Meas.* **2023**, *72*, 3293552.
204. Li, X.; Li, H.; Lin, Y.; Guo, J.; Yang, J.; Yue, H.; Li, K.; Li, C.; Cheng, Z.; Hu, H.; et al. Learning-based denoising for polarimetric images. *Opt. Express* **2020**, *28*, 16309–16321. [[CrossRef](#)] [[PubMed](#)]
205. Hu, H.; Huang, Y.; Li, X.; Jiang, L.; Che, L.; Liu, T.; Zhai, J. UCRNet: Underwater color image restoration via a polarization-guided convolutional neural network. *Front. Mar. Sci.* **2022**, *9*, 1031549. [[CrossRef](#)]
206. Qi, P.; Li, X.; Han, Y.; Zhang, L.; Xu, J.; Cheng, Z.; Liu, T.; Zhai, J.; Hu, H. U2R-pGAN: Unpaired underwater-image recovery with polarimetric generative adversarial network. *Opt. Lasers Eng.* **2022**, *157*, 107112. [[CrossRef](#)]
207. Liu, X.; Li, X.; Chen, S.C. Enhanced polarization demosaicking network via a precise angle of polarization loss calculation method. *Opt. Lett.* **2022**, *47*, 1065–1068. [[CrossRef](#)]

208. Li, Y.; Ma, L.; Zhong, Z.; Liu, F.; Chapman, M.A.; Cao, D.; Li, J. Deep learning for Lidar point clouds in autonomous driving: A review. *IEEE Trans. Neural Netw. Learn. Syst.* **2020**, *32*, 3412–3432. [CrossRef]
209. Hu, H.; Yang, S.; Li, X.; Cheng, Z.; Liu, T.; Zhai, J. Polarized image super-resolution via a deep convolutional neural network. *Opt. Express* **2023**, *31*, 8535–8547. [CrossRef] [PubMed]
210. Huang, Z.; Dong, Q.; Chen, B.; Wang, T.; Bi, J.; Zhou, T.; Alam, K.; Shi, J.; Zhang, S. Method for retrieving range-resolved aerosol microphysical properties from polarization Lidar measurements. *Opt. Express* **2023**, *31*, 7599–7616. [CrossRef]
211. Di Noia, A.; Hasekamp, O.; Van Harten, G.; Rietjens, J.; Smit, J.; Snik, F.; Henzing, J.; De Boer, J.; Keller, C.; Volten, H. Use of neural networks in ground-based aerosol retrievals from multi-angle spectropolarimetric observations. *Atmos. Meas. Tech.* **2015**, *8*, 281–299. [CrossRef]
212. Di Noia, A.; Hasekamp, O.P.; Wu, L.; van Diedenhoven, B.; Cairns, B.; Yorks, J.E. Combined neural network/Phillips—Tikhonov approach to aerosol retrievals over land from the NASA Research Scanning Polarimeter. *Atmos. Meas. Tech.* **2017**, *10*, 4235–4252. [CrossRef]
213. Eyeonic Vision System The Industry’s Most Compact, Powerful Coherent Machine Vision Solution. Available online: <https://www.silc.com/product/> (accessed on 3 September 2023).
214. Li, X.; Hu, H.; Zhao, L.; Wang, H.; Han, Q.; Cheng, Z.; Liu, T. Pseudo-polarimetric method for dense haze removal. *IEEE Photonics J.* **2019**, *11*, 1–11. [CrossRef]
215. Hu, H.; Qi, P.; Li, X.; Cheng, Z.; Liu, T. Underwater imaging enhancement based on a polarization filter and histogram attenuation prior. *J. Phys. Appl. Phys.* **2021**, *54*, 175102. [CrossRef]
216. Hu, H.; Lin, Y.; Li, X.; Qi, P.; Liu, T. IPLNet: A neural network for intensity-polarization imaging in low light. *Opt. Lett.* **2020**, *45*, 6162–6165. [CrossRef] [PubMed]
217. Li, X.; Xu, J.; Zhang, L.; Hu, H.; Chen, S.C. Underwater image restoration via Stokes decomposition. *Opt. Lett.* **2022**, *47*, 2854–2857. [CrossRef]
218. Xin, Z.; Changrui, Q.; Jianfeng, S.; Jiang, P.; Qi, W. Research on triggering properties enhancement of polarization detection geiger-mode APD LIDAR. *J. Quant. Spectrosc. Radiat. Transf.* **2020**, *254*, 107182.
219. Lio, G.E.; Ferraro, A. LIDAR and beam steering tailored by neuromorphic metasurfaces dipped in a tunable surrounding medium. *Photonics* **2021**, *8*, 65. [CrossRef]
220. Kim, I.; Martins, R.J.; Jang, J.; Badloe, T.; Khadir, S.; Jung, H.Y.; Kim, H.; Kim, J.; Genevet, P.; Rho, J. Nanophotonics for light detection and ranging technology. *Nat. Nanotechnol.* **2021**, *16*, 508–524. [CrossRef]
221. Kim, G.; Kim, Y.; Yun, J.; Moon, S.W.; Kim, S.; Kim, J.; Park, J.; Badloe, T.; Kim, I.; Rho, J. Metasurface-driven full-space structured light for three-dimensional imaging. *Nat. Commun.* **2022**, *13*, 5920. [CrossRef]
222. Juliano Martins, R.; Marinov, E.; Youssef, M.A.B.; Kyrou, C.; Joubert, M.; Colmagro, C.; Gâté, V.; Turbil, C.; Coulon, P.M.; Turover, D.; et al. Metasurface-enhanced light detection and ranging technology. *Nat. Commun.* **2022**, *13*, 5724. [CrossRef]
223. Liang, Y.; Lin, H.; Koshelev, K.; Zhang, F.; Yang, Y.; Wu, J.; Kivshar, Y.; Jia, B. Full-stokes polarization perfect absorption with diatomic metasurfaces. *Nano Lett.* **2021**, *21*, 1090–1095. [CrossRef]
224. Rubin, N.A.; D’Aversa, G.; Chevalier, P.; Shi, Z.; Chen, W.T.; Capasso, F. Matrix Fourier optics enables a compact full-Stokes polarization camera. *Science* **2019**, *365*, eaax1839. [CrossRef]

**Disclaimer/Publisher’s Note:** The statements, opinions and data contained in all publications are solely those of the individual author(s) and contributor(s) and not of MDPI and/or the editor(s). MDPI and/or the editor(s) disclaim responsibility for any injury to people or property resulting from any ideas, methods, instructions or products referred to in the content.